

1
2
3
4
5
6
7
8
9
10
11
12
13
14
15
16
17
18
19
20

Adjusting particle-size distributions to account for aggregation in tephra-deposit model forecasts

Larry G. Mastin¹, Alexa R. Van Eaton¹, and Adam J. Durant^{2,3}

[1] [U.S. Geological Survey, Cascades Volcano Observatory, 1300 SE Cardinal Court, Bldg. 10, Suite 100, Vancouver, Washington, USA, lgmastin@usgs.gov]

[2] [Section for Meteorology and Oceanography, Department of Geosciences, University of Oslo, Blindern, 0316 Oslo, Norway]

[3] [Geological and Mining Engineering and Sciences, Michigan Technological University, 1400 Townsend Drive, Houghton, MI 49931, USA]

Submitted to *Atmospheric Chemistry and Physics*, January 2016

21 **Abstract**

22 Volcanic ash transport and dispersion models (VATDs) are used to forecast tephra deposition
23 during volcanic eruptions. Model accuracy is limited by the fact that fine ash aggregates
24 (clumps into clusters), altering patterns of deposition. In most models this is accounted for by
25 *ad hoc* changes to model input, representing fine ash as aggregates with density ρ_{agg} , and a log-
26 normal size distribution with median μ_{agg} and standard deviation σ_{agg} . Optimal values may
27 vary between eruptions. To test the variance, we used the Ash3d tephra model to simulate four
28 deposits: 18 May 1980 Mount St. Helens; 16-17 September 1992 Crater Peak (Mount Spurr);
29 17 June 1996 Ruapehu; and 23 March 2009 Mount Redoubt. In 192 simulations, we
30 systematically varied μ_{agg} and σ_{agg} , holding ρ_{agg} constant at 600 kg m^{-3} . We evaluated the fit
31 using three indices that compare modeled versus measured (1) mass load at sample locations;
32 (2) mass load versus distance along the dispersal axis; and (3) isomass area. For all deposits,
33 under these inputs, the best-fit value of μ_{agg} ranged narrowly between $\sim 2.3\text{-}2.7\phi$ (0.20-0.15
34 mm), despite large variations in erupted mass (0.25-50Tg), plume height (8.5-25 km), mass
35 fraction of fine (<0.063 mm) ash (3-59%), atmospheric temperature, and water content between
36 these eruptions. This close agreement suggests that aggregation may be treated as a discrete
37 process that is insensitive to eruptive style or magnitude. This result offers the potential for a
38 simple, computationally-efficient parameterization scheme for use in operational model
39 forecasts. Further research may indicate whether this narrow range also reflects physical
40 constraints on processes in the evolving cloud.

41 **Keywords**

42 volcanic ash, volcanic plume, ash clouds, aerosols, aggregation, volcanic eruptions, tephra
43 deposition

44

45 **1 Introduction**

46 Airborne tephra is the most wide-reaching of volcanic hazards. It can extend hundreds to
47 thousands of kilometers from a volcano and impact air quality, transportation, crops, electrical
48 infrastructure, buildings, water supplies, and sewerage. During eruptions, communities want
49 to know whether they may receive tephra and how much might fall. Volcano observatories
50 typically forecast areas at risk by running volcanic ash transport and dispersion models

51 (VATD). As input, these models require information including eruption start time, plume
52 height, duration, the wind field, and the size distribution of the falling particles. Of these inputs,
53 the particle size distribution is perhaps the hardest to constrain.

54 Particle size (along with shape and density) determines settling velocity, which controls where
55 particles land in a given wind field. For different eruptions, the total particle-size distribution
56 (TPSD) can vary. Large eruptions produce more fine ash than small ones for example; and
57 silicic eruptions produce more than mafic (Rose and Durant, 2009). The TPSD is difficult to
58 estimate (e.g., Bonadonna and Houghton, 2005); hence estimates exist for only a handful of
59 deposits. And even in cases where the TPSD is known, that TPSD, entered into a dispersion
60 model, will not accurately calculate the pattern of deposition (Carey, 1996).

61 This inaccuracy results from the fact that complex processes, not considered in models, cause
62 particles to fall out faster than theoretical settling velocities would predict. These processes
63 include scavenging by hydrometeors (Rose et al., 1995a), gravitational instabilities that cause
64 dense clouds to collapse *en masse* (Carazzo and Jellinek, 2012; Schultz et al., 2006; Durant,
65 2015; Manzella et al., 2015), and aggregation, in which ash particles smaller than a few hundred
66 microns clump into clusters. The rate of aggregation, and the type and size of resulting
67 aggregates, depend on atmospheric processes such as ice accretion, electrostatic attraction, or
68 liquid-water binding whose importance varies from place to place.

69 Although one VATD model, Fall3d, calculates aggregation during transport for research studies
70 (Folch et al., 2010; Costa et al., 2010), no operational models consider it. Instead, aggregation
71 is accounted for by either setting a minimum settling velocity in the code (Carey and
72 Sigurdsson, 1982; Hurst and Turner, 1999; Armienti et al., 1988; Macedonio et al., 1988), or,
73 in the model input, adjusting particle size distribution by replacing some of the fine ash with
74 aggregates of a specified density, shape, and size range (Bonadonna et al., 2002; Cornell et al.,
75 1983; Mastin et al., 2013b). These strategies will probably prevail for at least the next few
76 years, until microphysical algorithms replace them.

77 These adjustments are mostly derived from *a posteriori* studies, where model inputs have been
78 adjusted until results match a particular deposit. It is unclear how well the optimal adjustments
79 might vary from case to case. For model forecasts during an eruption, we need some
80 understanding of this variability. This paper addresses this question, using deposits from four
81 well-documented eruptions. We derive a scheme for adjusting TPSD to account for

82 aggregation, optimize parameter values to match each deposit, and then see how much these
83 optimal values vary from one deposit to the next.

84 **2 Background on the deposits**

85 The IAVCEI Commission on Tephra Hazard Modeling has posted data from eight well-mapped
86 eruption deposits, available for use by modeling groups to validate VATD simulations
87 (<http://dbstr.ct.ingv.it/iavcei/>). Of these, we focus on eruptions that lasted for hours (not days);
88 where the TPSD included at least a few percent of ash finer than 0.063 mm in diameter; and
89 where data were available from distal (>35 km) sample locations. Four eruptions met these
90 criteria: the 18 May 1980 eruption of Mount St. Helens, 16-17 June 1996 eruption of Ruapehu,
91 and the 16-17 September and 18 August 1992 eruptions of Crater Peak (Mount Spurr), Alaska.
92 The August Crater Peak eruption was already studied using Ash3d (Schwaiger et al., 2012) and
93 therefore not included here, reducing the total to three. To these we add event 5 from the 23
94 March 2009 eruption of Mount Redoubt, Alaska. Although an Ash3d study was made of this
95 event (Mastin et al., 2013b), aggregation has been unusually well characterized in recent years
96 (Wallace et al., 2013; Van Eaton et al., in press).

97 Below are key observations of these events. Deposit maps are shown in Fig. 1, digitized from
98 published sources.

99 **1) The 18 May 1980 deposit from Mount St. Helens** remains among the best documented of
100 any in recent decades (Durant et al., 2009; Sarna-Wojcicki et al., 1981; Waitt and Dzurisin,
101 1981; Rice, 1981). This 9 hour eruption expelled magma that was dacitic in bulk composition
102 but contained about 40% crystals and 60% rhyolitic glass (Rutherford et al., 1985). The
103 eruption start time (1532 UTC) and duration are well documented (Foxworthy and Hill, 1982);
104 the time-changing plume height was tracked by Doppler radar (Harris et al., 1981) and satellite
105 (Holasek and Self, 1995) (Table 2). The deposit was mapped within days, before modification
106 by wind or rainfall, to a distance of ~800 km and to mass load values as low as a few hundredths
107 of a kilogram per square meter (Sarna-Wojcicki et al., 1981). Estimated volume of the fall
108 deposit in dense-rock equivalent (DRE) is 0.2 km³ (Sarna-Wojcicki et al., 1981) based on what
109 fell in the mapped area. A TPSD was estimated by Carey and Sigurdsson (1982) and later by
110 Durant et al. (2009) to contain about 59% ash <63 um in diameter (Table S1), with a modal
111 peak in particle size that coincided with the median bubble size of tephra fragments (Genareau
112 et al., 2012). Some fine ash may have been milled in pyroclastic density currents on the
113 afternoon of 18 May and in the lateral blast that morning. A secondary maximum in deposit

114 thickness in Ritzville, Washington (~290 km downwind) was inferred by Carey and Sigurdsson
115 (1982) to have resulted from fine ash aggregating and falling *en masse*, perhaps as the cloud
116 descended and warmed to above-freezing temperatures (Durant et al., 2009). Wind directions
117 that were more southerly at low elevations combined with elutriation off pyroclastic flows in
118 the afternoon to feed low clouds, producing a deposit that was richer in fine ash along its
119 northern boundary than in the south (Waite and Dzurisin, 1981; Eychenne et al., 2015).
120 Aggregates sampled by Sorem (1982) in eastern Washington consisted mainly of dry clusters
121 0.250 to 0.500 mm in diameter, containing particles <0.001 mm to more than 0.040 mm in
122 diameter, though no aggregates were visible in the fall deposit except at proximal locations (e.g.
123 Sisson (1995)). The eruption began under clear weather conditions. Clouds increased
124 throughout the day. Some precipitation in the form of mud rain was noted within tens of
125 kilometers of the vent (Rosenbaum and Waite, 1981), probably due to entrainment and
126 condensation of atmospheric moisture in the rising plume. But no precipitation was recorded
127 at more distal locations during the event.

128 **2) The 16-17 September 1991 eruption from Crater Peak, Mount Spurr, Alaska**, was the
129 third that summer from this vent. The eruption start time (0803 UTC September 17) and
130 duration (3.6 hours (Eichelberger et al., 1995)) were seismically constrained. The maximum
131 plume height, measured by U.S. National Weather Service radar (Rose et al., 1995b) increased
132 for the first 2.3 hours and then fluctuated between about 11 and 14 km above mean sea level
133 (MSL) until the plume height abruptly decreased at 1110 UTC. The andesitic tephra consisted
134 of two main types; tan and gray, which were both noteworthy for their low vesicularity (~20-
135 45%) and high crystallinity (40-100%) (Gardner et al., 1998). The deposit was mapped rapidly
136 after the eruption (Neal et al., 1995; McGimsey et al., 2001) to a distance of 380 km and mass
137 loads as low as 0.050 kg m⁻². This deposit displays a weak secondary thickness maximum 260-
138 330 km downwind. Durant and Rose (2009) derived a TPSD for this deposit, estimating about
139 40% smaller than 0.063 mm. Milling in proximal pyroclastic flows that accompanied this
140 eruption (Eichelberger et al., 1995) could have contributed fine ash. The eruption occurred at
141 night under clear skies (Neal et al., 1995).

142 **3) The 17 June 1996 eruption of Ruapehu** produced a classic weak plume that was modeled
143 by Bonadonna et al. (2005), Hurst and Turner (1999), Scollo et al. (2008), Liu et al. (2015), and
144 Klawonn et al. (2014), among others. The main phase involved two pulses, one beginning 16
145 June at 1910 UTC and lasting 2.5 hours, and the second at 2300 UTC and lasting approximately

146 1.5 to 2 hours. Ash-laden plumes reached to about 8.5 km altitude above MSL based on satellite
147 infrared images (Prata and Grant, 2001). The deposit was mapped out to the Bay of Plenty
148 (190 km), sampled at 118 locations to mass loads less than 0.01 kg m^{-2} , and yielded a total mass
149 of about 0.001 km^3 DRE (Bonadonna and Houghton, 2005). Ejecta consisted mainly of scoria
150 containing 75% glass and 25% crystals, with glass containing about 54 wt% SiO_2 (Nakagawa
151 et al., 1999). A TPSD estimate based on the Voronoi tessellation method (Bonadonna and
152 Houghton, 2005) suggested that ash $<0.063 \text{ mm}$ composed only about 3% of the deposit. A
153 minor secondary thickness maximum was constrained by mapping at about 160 km downwind
154 (Bonadonna et al., 2005) (Fig. 1c). Although some witnesses at distal locations observed loose,
155 millimeter-sized clusters falling, no aggregates or accretionary lapilli were present in the
156 deposit (Klawonn et al., 2014). The eruption was not accompanied by significant pyroclastic
157 density currents and occurred during clear weather.

158 **4) Event 5 of the 23 March 2009 eruption of Redoubt Volcano, Alaska** erupted through a
159 glacier and entrained a variable amount of water into a high-latitude early-spring atmosphere.
160 It began at 1230 UTC, lasted about 20 minutes on the seismic record (Buurman et al., 2013),
161 and sent a plume briefly to about 18 km as seen in both National Weather Service NEXRAD
162 Doppler radar from Anchorage, and a USGS mobile C-band radar system in Kenai, Alaska
163 (Schneider and Hoblitt, 2013). Within a few days after the eruption, the deposit was mapped
164 by its contrast with underlying snow in satellite images (NASA MODIS), and sampled for mass
165 load and particle size distribution at 38 locations, at distances up to $\sim 250 \text{ km}$ and mass loads as
166 low as 0.01 kg m^{-2} (Wallace et al., 2013). During Ash3d modeling of this eruption, Mastin et
167 al. (2013b) found that wind vectors varied rapidly with both altitude and time, making the
168 dispersal direction highly sensitive to both the plume height (which varied from ~ 12 to 18 km
169 during the 20-minute eruption) and the vertical distribution of mass in the plume. In the deposit,
170 Wallace et al. (2013) described abundant frozen aggregates with size decreasing with distance
171 from the vent, from about 10 mm at 12 km distance. Schneider et al. (2013) attributed the high
172 ($>50 \text{ dBZ}$) reflectivity of the proximal plume in radar images, and a rapid decrease in maximum
173 plume height over a period of minutes, to formation and fallout of ashy hail hydrometeors in
174 the rising column. Van Eaton et al. (2015) combined analysis of the aggregate microstructures
175 with a 3-D large-eddy simulation to show that the ash aggregates grew directly within the
176 volcanic plume from a combination of wet growth and freezing, in a process similar to hail
177 formation.

178 These eruptions vary from weak (Ruapehu) to strong (Redoubt) plumes, from mid-latitude (St.
179 Helens, Ruapehu) to high-latitude (Spurr, Redoubt), from dry (Ruapehu) to relatively wet
180 (Redoubt), from basaltic andesite (Ruapehu) to dacite (St. Helens), and from ~3% to 59% ash
181 <0.063 mm in diameter. Inferred aggregation processes range from dry (Ruapehu) to wet within
182 the downwind cloud (St. Helens), to liquid+ice in the rising column (Redoubt).

183 **3 Methods**

184 **3.1 The Ash3d model**

185 We model these eruptions using Ash3d (Schwaiger et al., 2012; Mastin et al., 2013a), an
186 Eulerian model that calculates tephra transport and deposition through a 3-D, time-changing
187 wind field. Ash3d calculates transport by setting up a three dimensional grid of cells, adding
188 tephra into the column of source cells above the volcano, and distributing the mass in the
189 column following the probability density function of Suzuki (Suzuki, 1983), modified by
190 Armienti et al. (Armienti et al., 1988)

$$191 \quad \frac{dQ_m}{dz} = Q_m \frac{k^2 (1 - z/H_v) \exp(k(z/H_v - 1))}{H_v [1 - (1 + k) \exp(-k)]}, \quad (1)$$

192 where Q_m is the mass eruption rate, H_v is plume height above the vent, z is elevation (above the
193 vent) within the plume, and k is a constant that adjusts the mass distribution. Suzuki (Suzuki,
194 1983) defines this function as a “probability density of diffusion” of mass from the column as
195 particles fall out. Here we regard it as a simplified parameterization of mass distribution with
196 no implication for physical process.

197 At each time step, tephra transport is calculated through advection by wind, through turbulent
198 diffusion, and through particle settling. For wind advection, simulations of Mount St. Helens,
199 Crater Peak, and Redoubt use a wind field obtained from the National Oceanic and Atmospheric
200 Administration’s (NOAA’s) NCEP/NCAR Reanalysis 1 model (“RE1”) (Kalnay et al., 1996).
201 For the Ruapehu simulations we used a local 1-D wind sounding, which gave more accurate
202 results as detailed below. The RE1 model provides wind vectors on a global 3-D grid spaced
203 at 2.5° latitude and longitude, and 17 pressure levels in the atmosphere (1000-10 hPa), updated
204 at 6-hour intervals. Ash3d calculates turbulent diffusion using a specified diffusivity D
205 (Schwaiger et al., 2012, Eq. 4). D is set to zero for simplicity, though later we show the effect
206 of different values of D .

207 Settling rates are calculated using relations of Wilson and Huang (1979) for ellipsoidal particles.
208 Wilson and Huang define a particle shape factor $F \equiv (b + c)/2a$, where a , b , and c are the
209 maximum, intermediate, and minimum diameters of the ellipsoid respectively. Wilson and
210 Huang measured a , b , and c for 155 natural pyroclasts. From data published in Wilson and
211 Huang, we calculate an average F of 0.44, which we use in our model. For aggregates we use
212 $F=1.0$ (round aggregates).

213 Other model inputs include the extent and nodal spacing of the model domain; vent location
214 and elevation; the eruption start time, duration, plume height, erupted volume, diffusion
215 coefficient D , and a series of particle size classes and associated densities. The size classes
216 may represent either individual particles or aggregates. These input values are given in Tables
217 1 and 2.

218 **3.2 Adjusting particle size distributions to account for aggregation**

219 In deriving a particle size adjustment scheme we found it necessary to prioritize the type(s) of
220 processes and products we wish to replicate. The rate and type of ash aggregation are known
221 to vary with both eruptive conditions and meteorology. Large aggregates, including frozen
222 accretionary lapilli, form near the source and are abundant in phreatomagmatic deposits (Van
223 Eaton et al., 2015; Brown et al., 2012; Houghton et al., 2015). They are associated with particles
224 colliding in moist, turbulent updrafts within a rising plume (Fig. 2) or an elutriating ash cloud.
225 These near-source aggregates commonly exceed 1 cm diameter (Wallace et al., 2013; Swanson
226 et al., 2014; Van Eaton and Wilson, 2013). In contrast, the low-density aggregates that produced
227 the Ritzville Bulge, 230 km downwind from Mount St. Helens, are thought to have been
228 triggered by mammatus cloud instabilities (Durant et al., (2009)) as the cloud descended,
229 warmed, and ice melted into liquid water (red line, Fig. 2). These aggregates tend to be smaller
230 than a millimeter, and form in the cloud hundreds of kilometers downwind from source (Sorem,
231 1982; Dartayat, 1932). At Mount St. Helens and perhaps other places, investigators found
232 evidence for both large, wet, proximal accretionary lapilli (Sisson, 1995) and distal, dry
233 aggregates (Sorem, 1982). The latter type deposited over a larger area, involved a greater
234 fraction of the total erupted mass, and affected a greater population. Thus it is the latter process
235 whose deposits we wish to reproduce.

236 Aggregation is also a highly size-selective process. The threshold size below which most
237 particles aggregate and above which they don't varies with moisture and electrical charge,

238 ranging from several tens of microns under dry conditions, to hundreds of microns when liquid
239 water is present (Gilbert and Lane, 1994; Schumacher and Schmincke, 1995; Van Eaton et al.,
240 2012). Our aggregation scheme is too crude to distinguish the threshold size as a function of
241 atmospheric conditions, hence we use a broad range such that:

242 For $\phi \geq 4$, all ash aggregates

243 For $\phi \leq 2$, no ash aggregates.

244 For $4 > \phi > 2$, the mass fraction that aggregates varies linearly with ϕ from 1 (when $\phi = 4$) to 0
245 (when $\phi = 2$).

246 The TPSD used to model these four eruptions are listed in Table S1 and illustrated as gray bars
247 in Fig. 3. Particle sizes that do not aggregate according to this scheme are illustrated as black
248 bars. We assume that the aggregates collect into clusters having a Gaussian size distribution of
249 mean μ_{agg} , and standard deviation σ_{agg} (insets, Fig. 3). For deposit modeling, we ignore the
250 small fraction of the erupted mass that goes into the distal cloud, typically a few percent (Dacre
251 et al., 2011; Devenish et al., 2012).

252 In our study, the aggregated ash mostly deposits as a secondary thickness maximum. Different
253 choices of a threshold size for particle aggregation would influence the mass building the
254 secondary maximum. For Mount St. Helens, about 10% of the erupted mass lies between $\phi = 2$
255 and $\phi = 4$. For Spurr, Ruapehu, and Redoubt, the percentages are 28%, 6% and 11%. These
256 values reflect the variability in mass of the secondary maximum that could result from different
257 choices of the aggregation-size threshold.

258 **Aggregate Density:** Different processes influence aggregate density. Wet ash (>10-15 wt.%
259 liquid water) rapidly produces sub-spherical pellets with density $> 1,000 \text{ kg m}^{-3}$ (Schumacher
260 and Schmincke, 1991; Van Eaton et al., 2012); drier conditions lead to electrostatically-bound
261 clusters (Schumacher and Schmincke, 1995; Van Eaton et al., 2012) with density in the
262 hundreds of kilograms per cubic meter range (James et al., 2002; Taddeucci et al., 2011).
263 Taddeucci et al. (2011) estimated densities ranging from < 100 to $> 1,000 \text{ kg m}^{-3}$ in dry
264 aggregates photographed falling 7 km from the Eyjafjallajökull vent. For simplicity, we hold
265 ρ_{agg} constant at 600 kg m^{-3} , toward the middle of the observed range but higher than that of
266 some dry aggregates. Optimal aggregate sizes that we derive later in this paper are determined
267 by this assumed density, and may be larger or smaller than actual aggregate sizes.

268 3.3 Statistical measures of fit

269 For each eruption, we have done a series of model simulations, first using the TPSD without
270 considering aggregation, and then systematically varying σ_{agg} and μ_{agg} to include the effects of
271 aggregation. We compare the resulting modeled deposit with the mapped deposit using three
272 methods presented in Table 3. Each has advantages and disadvantages.

273 1) **The point-by-point index** Δ^2 compares model results with sample data collected at specific
274 locations (dots, Fig. 1). It offers the advantage that the comparison is made directly with
275 measured values, not with interpreted or extrapolated contours of data. But Δ^2 can be influenced
276 by errors in the wind field, which cannot be adjusted in the model. More importantly, Δ^2 can
277 be dominated by differences in proximal locations where mass per unit area is greatest, and
278 where near-vent processes, such as fallout from the vertical column, are not accurately
279 simulated. For these reasons, we exclude proximal data, within a few column heights distance
280 from the vent, from the calculation of Δ^2 .

281 2) **The downwind thinning index** $\Delta_{downwind}^2$, compares modeled mass per unit area along the
282 downwind dispersal axis with values expected at that distance based on a trend line drawn from
283 field measurements (Fig. 4). The comparison is not made directly with measured values (a
284 disadvantage). However the method does not suffer the limitation of over-weighting proximal
285 data. And, more importantly, it still provides a useful comparison when wind errors cause the
286 modeled dispersal axis to diverge from the mapped one.

287 3) **The isomass area index** Δ_{area}^2 compares the area within modeled and mapped isomass
288 lines. It is based on traditional plots of the log of isopach thickness versus square root of area
289 (Pyle, 1989; Fierstein and Nathenson, 1992; Bonadonna and Costa, 2012), which are assumed
290 to accurately depict the areal distribution of tephra while minimizing the effects of 3-D wind
291 on the distribution (Pyle, 1989). Fig. 5 shows plots for our four eruptions, using the log of
292 isomass rather than isopach thickness to avoid problems introduced by varying deposit density.

293 The index Δ_{area}^2 is assumed to be insensitive to effects of wind (an advantage). However,
294 model results are compared with isopach lines that are interpretive and may not be well
295 constrained, depending on the distribution and number density of sample locations.

296 3.4 Sensitivity to various input values

297 We ignore complex, proximal fallout and concentrate on medial to distal areas, about 100 to
298 ~500 km downwind at Mount St. Helens, for example. There, under the average wind speed
299 (15.1 m s^{-1}) that existed below about 15 km, tephra falling from 15 km at average settling
300 velocities of $0.4\text{-}1.5 \text{ m s}^{-1}$ would deposit within this range (Fig. 6a). Tephra falling at $0.66\text{-}0.78$
301 m s^{-1} would land 290-340 km downwind, the distance of the secondary maximum at Ritzville.
302 A wide range of aggregate diameters d could fall at this rate depending on density ρ_{agg} (Fig.
303 6b).

304 Other factors listed below can also affect the results.

305 **Aggregate shape.** Aggregate shape can strongly affect the settling velocity and thus where
306 deposits fall, as illustrated in Fig. 7. For simplicity, we use round aggregates ($F=1.0$).

307 **Suzuki k .** Simulations of Mount St. Helens (Fig. 8) show that increasing the Suzuki factor from
308 4 to 8 increases the prominence of a secondary thickness maximum. But at $k \sim 8$, the proximal
309 deposit becomes unrealistically thin. Our simulations use $k=8$ to replicate the known prominent
310 secondary thickening while minimizing unrealistic thinning of proximal deposits.

311 **Aggregate size.** The transport distance is highly sensitive to aggregate size. Reducing
312 aggregate diameter d from 0.250 to 0.217 to 0.189 mm increases transport distance at Mount
313 St. Helens from 300 to 366 to 448 km respectively (Fig. 6a). In simulations that use a single,
314 dominant aggregate size, these variations produce conspicuous changes in the location of a
315 secondary maximum (Fig. 9). Decreasing size also decreases the percent of erupted mass that
316 lands in the area shown in Fig. 9: from 63% to 35% to 15% for $d=0.165, 0.143, \text{ and } 0.125 \text{ mm}$
317 respectively ($\phi=2.6, 2.8, 3.0$). At $d=0.1 \text{ mm}$ ($\phi=3.3$), only 4% of the erupted mass lands in the
318 mapped area.

319 This constrains the range of aggregate sizes we may use in our simulations. Sparse observations
320 suggest that $>90\%$ of erupted mass falls as an observable deposit while less than several percent
321 is transported downwind as a distal cloud (Wen and Rose, 1994; Devenish et al., 2012). To
322 ensure a similar relationship in our simulations, nearly all of the aggregate-size distribution
323 must be coarser than about 0.1 mm. At the proximal end, for Mount St. Helens, Durant et al.
324 (2009) found that most fine ash fell at distances $>150 \text{ km}$. This implies aggregate sizes coarser
325 than about 0.32 mm ($\phi=1.6$) (Figs 6, 9). To ensure that the tails of our aggregate-size
326 distribution land in the area of interest, we must vary μ_{agg} values within a narrow range of about

327 1.9-3.1 ϕ (0.27-0.12 mm), and σ_{agg} within a small fraction of this range. We assume that similar
328 constraints apply to all deposits in this study.

329 **Fall-velocity model.** Different fall-velocity models are used in different tephra dispersion
330 models. These models give slightly different results, and it should be noted that our results are
331 specific to our choice of the Wilson and Huang fall model.

332 Finally, we note that key parameters such as particle density, shape, Suzuki k etc. are held
333 constant for all four eruptions even though they may vary from one eruption to another. Such
334 parameters cannot easily be scrutinized when setting up simulations during an eruption. An
335 objective is to see how well “standard” values, even if locally unrealistic, can reproduce
336 observations.

337

338 4 Results

339 We ran simulations at $\mu_{agg} = 1.9, 2.0, 2.1 \dots 3.1\phi$, and $\sigma_{agg} = 0.0, 0.1, 0.2, \text{ and } 0.3\phi$. The latter
340 used 1, 5, 7, and 11 aggregate size classes respectively, in each simulation, with the percentage
341 of fine ash assigned to each bin given in Table 4. Our calculations of Δ^2 and $\Delta_{downwind}^2$ only
342 included sample points whose downwind distance lay within the range indicated by the trend
343 lines in Fig. 4.

344 Figure 10 shows contours of Δ^2 , $\Delta_{downwind}^2$, and Δ_{area}^2 as a function of σ_{agg} and μ_{agg} for each of
345 these four deposits. Values are given in Tables S3-S6. Although the three indices compare
346 different features of the deposit, they provide roughly similar optimal values of μ_{agg} . For
347 Mount St. Helens, for example, the best-fit value of μ_{agg} is about 2.4 ϕ using Δ^2 (Fig. 10a), 2.5 ϕ
348 using $\Delta_{downwind}^2$ (Fig. 10b), and 2.7 ϕ using Δ_{area}^2 (Fig. 10c). Optimal values of σ_{agg} are 0.1, 0.1,
349 and 0.2 respectively. For Crater Peak, optimal μ_{agg} values are 2.6 ϕ , 2.5 ϕ , and 2.0 ϕ respectively,
350 while for Ruapehu they are 2.3 ϕ , 2.5 ϕ , and 2.5 ϕ . For both Crater Peak and Ruapehu, optimal
351 values of σ_{agg} range from 0.0 to 0.2. For Redoubt, optimal values are disparate: $\mu_{agg} = 2.5\phi$,
352 2.5 ϕ , and $<2\phi$ respectively. The Redoubt deposit is least constrained by field data and the most
353 difficult to match due to the complex wind conditions.

354 Figures 11-14 show results for each of these eruptions using $\mu_{agg}=2.4\phi$ (0.19 mm) and σ_{agg}
355 $=0.1\phi$. The sizes of particles and aggregates used to generate these figures is given in Table
356 S2. For all deposits these values are close to optimal, depending on which criterion is used.
357 Similar figures for other values of μ_{agg} and σ_{agg} are provided as Figs. S005-S212.

358 Figures S001-S004 show simulations using the original particle-size distribution, with no
359 aggregation. Tephra fall beyond a few tens of kilometers is strongly underestimated in all these
360 runs, especially for the three eruptions that contain more than a few percent fine ash. Values
361 of Δ^2 , $\Delta_{downwind}^2$, and Δ_{area}^2 are also higher than most simulations that use aggregates (Table S3-
362 S6). For Mount St. Helens, Crater Peak, Ruapehu, and Redoubt, the percentages of the erupted
363 mass landing in the mapped area are very low: 29%, 42%, 88%, and 59% respectively.

364 Optimal aggregates obtained from our study are similar in size but denser than those found
365 optimal by Cornell et al. (1983) for the Campanian Y-5 ($\mu_{agg}=2.3\phi$, $\rho_{agg}=200 \text{ kg m}^{-3}$) deposit.
366 The unknown wind field during the prehistoric Campanian Y-5 eruption makes it difficult to
367 compare Cornell et al.'s optimal value to the results here. Folch et al. (2010) matched the
368 Mount St. Helens deposit using a similar aggregation scheme, but with aggregates of density
369 400 kg m^{-3} (compared with our 600 kg m^{-3}) and diameter of 0.2-0.3 mm (compared with our
370 $\sim 0.2 \text{ mm}$). Their results are broadly consistent with ours.

371 **4.1 Mount St. Helens**

372 For the Mount St. Helens case, the modeled deposit follows a dispersal axis (solid black line,
373 Fig. 11a) that matches almost exactly with the mapped one (dashed line). The agreement
374 reflects both the faithfulness of the numerical wind field to the true one and the appropriateness
375 of other inputs, such k , that influence dispersal direction. The measured mass loads in Fig. 11a,
376 indicated by the color of markers, agree reasonably well with modeled mass loads indicated by
377 colors of the contour lines, except along the most distal transect, where modeled loads are
378 essentially zero while measured loads are about $10^{-1} \text{ kg m}^{-2}$. Figure 11b shows that modeled
379 and measured mass loads generally agree within a factor of three or so, except for those same
380 distal, low-mass-load measurements, to the lower left of the legend label (those where modeled
381 values are truly zero do not show up on this plot). Figure 11c shows that the modeled mass
382 load (black line with dots) contains a secondary thickening at about the same location mapped
383 (dashed line). It also has roughly the same downwind shape, in contrast to results using $\sigma_{agg}=0.2$

384 and 0.3 (Figs. S027-S028), in which the secondary thickening is broader and thinner than
385 observed. However, the modeled mass load is consistently less than measured, especially at
386 the most distal sites. In Fig. 11d, the log of modeled mass load versus square root of area shows
387 reasonable agreement with mapped values until mass loads are less than about 1 kg m^{-2} , where
388 they diverge.

389 Notably, modeled mass loads somewhat underestimate the measured values along the dispersal
390 axis in Fig. 11c. The underestimate reflects the fact that the input erupted volume of 0.2 km^3
391 DRE (Table 1) was based on estimates by Sarna-Wojcicki et al. (1981) of what lay within the
392 mapped area in Fig. 11a; yet only about 78% of the modeled mass landed within this area.
393 Reducing the mean aggregate size to 2.6ϕ (0.164 mm , Fig. S036) improves the fit somewhat
394 along distal parts of the transect but degrades it near Ritzville. And the finer size moves the
395 secondary maximum too far east and reduces the percentage deposited to $\sim 65\%$.

396 In Fig. 11a, the modeled deposit is also slightly narrower than the mapped one. Adding
397 turbulent diffusion, with a diffusivity D of about $3 \times 10^2 \text{ m}^2 \text{ s}^{-1}$ (Fig. 15) visually improves the
398 fit, and was likely important during this eruption due to high crosswind speeds that increased
399 entrainment (Degruyter and Bonadonna, 2012; Mastin, 2014). But adding diffusion slightly
400 increases Δ^2 , improving fit on deposit margins at the expense of the axis. Ignoring turbulent
401 diffusion also decreases run time by $\sim 3x$, from ~ 30 to 10 minutes, yielding faster results under
402 operational conditions. Results with other models may vary depending on model setup and
403 configuration.

404 **4.2 Crater Peak (Mount Spurr)**

405 At Crater Peak (Mount Spurr), results in Fig. 12a also show good agreement between the
406 modeled dispersal axis and the mapped one (which is constrained by fewer sample locations
407 than the Mount St. Helens case). The isomass lines in this plot are jagged and irregular due to
408 effects of topography in this mountainous region. The modeled location of secondary
409 thickening in Fig. 12c agrees with the mapped location, about 250-300 km downwind.
410 Although Fig. 12c shows a tendency for the model to underestimate the mass load along the
411 dispersal axis, there is less tendency to underestimate mass load in the most distal locations as
412 occurred at Mount St. Helens. In Fig. 12d, the areas covered by modeled isomass lines are
413 comparable to the mapped values, down to mass loads approaching 0.1 kg m^{-2} .

414 4.3 Ruapehu

415 For Ruapehu (Fig. 13), simulations using the NCEP Reanalysis 1 numerical winds produced an
416 odd double dispersal axis whose average did not correspond well with the mapped direction of
417 dispersal (Fig. 1c). To improve the fit we used the 1-D wind sounding provided for this eruption
418 at the IAVCEI Tephra Hazard Modeling Commission web page (<http://dbstr.ct.ingv.it/iavcei/>).
419 Use of a 1-D wind sounding seems justified in this case because this deposit covers a smaller
420 area than the others, making a 3-D wind field less important in calculating transport. The
421 resulting dispersal axis (Fig. 13a) agrees with the mapped one out to about 140 km distance,
422 beyond which it strays eastward, reaching the coast, 180 km downwind, about 10 km east of
423 the mapped axis. This slight difference is enough to cause misfits in point-to-point comparisons
424 at measured mass loads of $\sim 10^{-1}$ kg m⁻² (Fig. 13b).

425 The modeled mass load along the dispersal axis (Fig. 13c) agrees with measurements to about
426 60-90 km distance. At 100-200 km, modeled values level off and show a hint of secondary
427 thickening at ~ 180 km, in agreement with the mapped deposit (Fig. 1c and 13c), although the
428 mapped secondary thickening is more prominent.

429 A large discrepancy is also apparent at distances of less than 60 km, where mass load along the
430 dispersal axis (Fig. 13c) and the area covered by thick isomass lines (Fig. 13d) are greater than
431 for the mapped deposit. The implication is that too much mass is dropping out proximally in
432 the model. Underestimates of isomass area at $\leq 10^{-1}$ kg m⁻² (Fig. 13d) also show that too little
433 is falling distally. Simulations (not shown) that raise the plume height or increase k to
434 concentrate more mass high in the plume do not improve the fit. The discrepancy may reflect
435 the coarse TPSD—50% of which is coarser than 1 mm (compared with 2%, 12%, and 8% for
436 the other three deposits in Table S1). An additional simulation used the TPSD derived from
437 technique B of Bonadonna and Houghton (2005) (Table S1), which divides the deposit into
438 arbitrary sectors, and calculates a weighted sum of the size distributions in each sector following
439 Carey and Sigurdsson (1982). Technique B yields a finer average particle size than technique
440 C, which uses Voronoi tessellation to sectorize the deposit. But the finer particle size of the
441 technique B TPSD does not improve the fit. Further exploration of this discrepancy is beyond
442 the scope of this paper; but other possible causes could include release of different particle sizes
443 at different elevations, or complex transport in the bending of the weak plume that can't be
444 accommodated in this model.

445 A second, smaller discrepancy is that the modeled deposit is narrower than the mapped one
446 (Fig. 1c). As at Mount St. Helens, deposit widening due to cross flow entrainment is likely.
447 Increases in entrainment resulting from crossflow is widely known to both increase plume width
448 and decrease its height for a given eruption rate (Briggs, 1984; Hault and Weil, 1972; Hewett
449 et al., 1971; Woodhouse et al., 2013). Adding turbulent diffusion, we get a visually improved
450 fit when $D \sim 3 \times 10^2 \text{ m}^2 \text{ s}^{-1}$ (Fig. 16), consistent with findings by Bonadonna et al. (2005) based
451 on the rate of downwind widening of isomass lines. This diffusivity is also similar to the visual
452 best-fit value for Mount St. Helens (Fig. 15).

453 Despite the uncertainty in TPSD, simulations that systematically vary μ_{agg} and σ_{agg} fit best in
454 Figs. 10g, h, and i when μ_{agg} is about 2.3 to 2.5. Results similar to those presented in Fig. 13c
455 use other values of μ_{agg} (Figs. S109-S160) and show a secondary maximum migrating
456 downwind as μ_{agg} increases, coming into agreement with the mapped distance at $\mu_{agg} = 2.3$ to
457 2.5ϕ (0.20-0.18 mm), where errors in Fig. 10g, h, and i are lowest.

458 **4.4 Redoubt**

459 This deposit is the second smallest in our group, the least well-constrained by sampling, and
460 the only one in our group not known to include a secondary thickness maximum. Mastin et al.
461 (2013b) modeled this deposit using numerical winds from the North American Regional
462 Reanalysis model (Mesinger et al., 2006). During that eruption, the winds at 0-4 km, 6-10, and
463 >10 km elevation were directed toward the northwest; north, and northeast respectively, with
464 the highest speeds at 6-10 km. Mastin et al. found that the modeled cloud developed a north-
465 oriented, northward migrating wishbone shape with the west prong at low elevation and the east
466 prong at high elevation. Mastin et al. also found that the modeled dispersal axis and the mass
467 load distribution roughly agreed with mapped values for a plume height of 15 km, $k=8$, and a
468 particle size adjustment that involved taking 95% of the fine ash (<0.063 mm) and distributing
469 it evenly among the coarser bins. In this study we use the same plume height and k value, a
470 different wind field (RE1), and explore a different parameterization for particle aggregation.

471 In Fig. 14a, the modeled dispersal axis diverges about 20° westward from the mapped axis. We
472 do not correct this divergence by adjusting mass height distribution, since the optimal values of
473 μ_{agg} and σ_{agg} can still be obtained from $\Delta_{downwind}^2$, and Δ_{area}^2 . As with the Crater Peak (Spurr)

474 simulations, the isomass lines are jagged and patchy; an artifact of high relief. (The most distal
475 sample location lies at 4.3 km elevation on the west shoulder of Mount Denali). Although the
476 value of μ_{agg} (2.4ϕ , 0.19 mm) portrayed in Fig. 14 is close to optimal in Fig. 10j, many sample
477 points do not plot in Fig. 14b because modeled mass load is zero. And most values of Δ^2 are
478 high—0.99, largely because of the disparity in axis dispersal directions and the consequent fact
479 that sample points lie outside the modeled deposit. The reason that Δ^2 shows a clear minimum,
480 around $\mu_{agg}=2.4\phi$ (0.19 mm) in Fig. 10j, is apparent from Figs. S161-S212 which show that,
481 as μ_{agg} decreases in size, the modeled deposit extends farther north and takes a clear turn to the
482 northeast, overlapping more with the mapped deposit. These figures also illuminate why
483 $\Delta_{downwind}^2$ is optimal at $\mu_{agg}=2.3$; because modeled and mapped loads come into best agreement
484 along the dispersal axis for aggregates of this size. Δ_{area}^2 is optimized at $\mu_{agg} < 2$ because the
485 area of the 1 kg m^{-2} isomass diverges below the mapped value, and the area of the 0.01 kg m^{-2}
486 isomass diverges above observed, as aggregate size increases. The isomass lines are drawn
487 based on sparse data and are the least reliable of the datasets used in this comparison.

488 **5 Discussion and Conclusions**

489 The overall derived values of μ_{agg} have a narrow range between ~ 2.3 - 2.7ϕ (0.15-0.20 mm),
490 despite large variations in erupted mass (0.25- $50\times Tg$), plume height (8.5-25 km), mass fraction
491 of fine (<0.063 mm) ash (3-59%), atmospheric temperature, and water content between these
492 eruptions. The value of this narrow range depends strongly on other inputs, such as particle
493 density, shape factor, and Suzuki factor. Values assigned here may not always be
494 representative. Aggregate density for example is frequently less than 600 kg m^{-3} . And different
495 assumptions on particle or aggregate shape could significantly change our results. Moreover,
496 our result is partly an artifact of our choice to optimize fit to deposits at medial distances of
497 several tens to hundreds of kilometers. Including more proximal sample points may have given
498 optimal aggregate sizes that spanned a wider range, as used for example in aggregation schemes
499 for Vesuvius (Barsotti et al., 2015) or Iceland (Biass et al., 2014). Despite these considerations,
500 the similarity in optimal values of μ_{agg} between these four eruptions is noteworthy.

501 The overall agreement in modeled mean aggregate size (μ_{agg}) suggests that accelerated fine-
502 ash deposition may be treated as a discrete process, insensitive to eruptive style or magnitude.

503 It seems unlikely that these varied eruptions would produce aggregates of the same size, density,
504 and morphology. A combination of processes removed ash. Our approach captures these
505 processes implicitly, ignoring the microphysics.

506 What sort of processes could evolve in the cloud? Some possibilities are illustrated in Fig. 2.
507 The evolution starts with ejection of particles from the vent, with size ranging from microns to
508 meters. For an eruption having the TPSD of Mount St. Helens, the rising plume would have
509 contained 10^6 - 10^8 particles per cubic meter with diameter between 10-30 μm that collided with
510 larger particles many times per second. High collision rates and the availability of liquid water
511 in the plume would have led to rapid aggregation. Freezing of liquid water and riming would
512 have shifted the maximum possible size of aggregates towards mm to cm sizes. Mud rain,
513 observed falling at Mount St. Helens (Waite, 1981) and ice aggregates collected near the vent
514 at Redoubt (Van Eaton et al., in press), are evidence of these processes.

515 In the downwind cloud particle concentrations were lower, turbulence was less intense, a
516 smaller range of particle sizes existed, and, for all four eruptions, atmospheric temperatures
517 near the plume top were well below freezing (Table 5), leading to presumably slow aggregation
518 rates. However, at least two other processes may help settle ash from downwind clouds. One
519 is gravitational overturn. Experiments (Carazzo and Jellinek, 2012) have observed that fine ash
520 settles toward the bottom of ash clouds as they expand and move downwind, accumulating
521 gravitationally unstable particle boundary layers that eventually overturn and cause the entire
522 air mass to settle rapidly. At Eyjafjallajökull in 2010, gravitational convective instabilities
523 formed within 10 km of the vent, presumably as a result of accumulation of coarse ash over a
524 period of minutes (Manzella et al., 2015). The development of fine-ash particle boundary layers
525 presumably takes longer, perhaps hours, although the underlying processes remain a subject of
526 active research.

527 A second process is hydrometeor growth. In some cases, magmatic and (or) externally-derived
528 water in the eruption cloud may condense on ash particles and initiate hydrometeor growth.
529 Both hydrometeor growth and gravitational overturn have been suggested to produce the
530 mammatus clouds that developed in mid-day over central Washington on 18 May 1980 and
531 signaled mass settling (Durant, 2015; Durant et al., 2009; Carazzo and Jellinek, 2012).
532 Mammatus descent rates are typically meters per second (Schultz et al., 2006), much faster than
533 the settling rate of individual ash particles ($<0.1 \text{ m s}^{-1}$) or even of ash aggregates ($<\sim 1 \text{ m s}^{-1}$,
534 Fig. 6).

535 The extent to which these processes operated at Crater Peak, Ruapehu, and Redoubt is
536 unknown. Cloud structures were not observed during the nighttime eruptions of Redoubt and
537 Crater Peak (Spurr). And although virga-like structures can be seen in some near-vent photos
538 of Ruapehu (Bonadonna et al., 2005, Fig. 9a), we have seen no documentation of such
539 instabilities farther downwind.

540 For operational forecasting, these mechanisms cannot be considered in any case, because no
541 operational model has the capability to resolve these processes. The fact that these eruptions
542 can all be reasonably modeled using similar inputs for aggregate size is convenient, even if the
543 processes involved are not specified in the model. The agreement suggests that model forecasts
544 can still be useful during the coming years. Future work will focus on the development of more
545 sophisticated algorithms that account for cloud microphysics.

546 **Author contributions**

547 L. Mastin conceived the study, did the model simulations and wrote most of the paper. A. Van
548 Eaton provided advice on aggregation processes. A. Durant provided the data for Mount St.
549 Helens and Crater Peak, and advice on aggregation processes that occurred during those two
550 eruptions.

551 **Acknowledgments**

552 We are grateful to the IAVCEI Commission on Tephra Hazard Modeling for posting data on
553 key eruptions that could be used for this study.

554 **References**

- 555 Armienti, P., Macedonio, G., and Pareschi, M. T.: A numerical model for simulation of tephra
556 transport and deposition: Applications to May 18, 1980, Mount St. Helens eruption, *J.*
557 *Geophys. Res.*, 93, 6463-6476, 1988.
- 558 Barsotti, S., Neri, A., Bertagnini, A., Cioni, R., Mulas, M., and Mundula, F.: Dynamics and
559 tephra dispersal of Violent Strombolian eruptions at Vesuvius: insights from field data,
560 wind reconstruction and numerical simulation of the 1906 event, *Bull. Volcanol.*, 77,
561 1-19, 10.1007/s00445-015-0939-6, 2015.
- 562 Biass, S., Scaini, C., Bonadonna, C., Folch, A., Smith, K., and Höskuldsson, A.: A multi-scale
563 risk assessment for tephra fallout and airborne concentration from multiple Icelandic
564 volcanoes – Part 1: Hazard assessment, *Nat. Hazards Earth Syst. Sci.*, 14, 2265-
565 2287, 10.5194/nhess-14-2265-2014, 2014.
- 566 Bonadonna, C., Macedonio, G., and Sparks, R. S. J.: Numerical modeling of tephra fallout
567 associated with dome collapses and Vulcanian explosions: application to hazard
568 assessment on Montserrat, in: the eruption of Soufriere Hills Volcano, Montserrat,
569 edited by: Druitt, T. H., and Kokelaar, B. P., Geological Society of London memoirs,
570 Geological Society of London, London, 517-537, 2002.
- 571 Bonadonna, C., and Houghton, B. F.: Total grain-size distribution and volume of tephra-fall
572 deposits, *Bull. Volcanol.*, 67, 441-456, 2005.
- 573 Bonadonna, C., Phillips, J. C., and Houghton, B. F.: Modeling tephra sedimentation from a
574 Ruapehu weak plume eruption, *J. Geophys. Res.*, 110, doi:10.1029/2004JB003515,
575 2005.
- 576 Bonadonna, C., and Costa, A.: Estimating the volume of tephra deposits: A new simple
577 strategy, *Geology*, 40, 415-418, 10.1130/g32769.1, 2012.
- 578 Briggs, G. A.: Plume rise and buoyancy effects, in: Atmospheric Science and Power
579 Production, edited by: Randerson, D., U.S. Department of Energy, Washington, D.C.,
580 327-366, 1984.
- 581 Brown, R. J., Bonadonna, C., and Durant, A. J.: A review of volcanic ash aggregation,
582 Physics and Chemistry of the Earth, Parts A/B/C, 45-46, 65-78,
583 <http://dx.doi.org/10.1016/j.pce.2011.11.001>, 2012.
- 584 Buurman, H., West, M. E., and Thompson, G.: The seismicity of the 2009 Redoubt eruption,
585 *J. Volcanol. Geotherm. Res.*, 259, 16-30, 2013.
- 586 Carazzo, G., and Jellinek, A. M.: A new view of the dynamics, stability and longevity of
587 volcanic clouds, *Earth Planet. Sci. Lett.*, 325-326, 39-51,
588 <http://dx.doi.org/10.1016/j.epsl.2012.01.025>, 2012.
- 589 Carey, S., and Sigurdsson, H.: Influence of particle aggregation on deposition of distal tephra
590 from the May 18, 1980, eruption of Mount St. Helens volcano, *J. Geophys. Res.*, 87,
591 7061-7072, 1982.
- 592 Carey, S., Sigurdsson, H., Gardner, J. E., and Criswell, W.: Variations in column height and
593 magma discharge during the May 18, 1980 eruption of Mount St. Helens, *J. Volcanol.*
594 *Geotherm. Res.*, 43, 99-112, 1990.
- 595 Carey, S.: Modeling of tephra fallout from atmospheric eruptions, in: Monitoring and
596 Mitigation of Volcanic Hazards, edited by: Scarpa, L. A., and Tilling, R. I., Springer
597 Verlag, Berlin, 429-463, 1996.
- 598 Cornell, W., Carey, S., and Sigurdsson, H.: Computer simulation of transport and deposition
599 of the campanian Y-5 ash, *J. Volcanol. Geotherm. Res.*, 17, 89-109, 1983.
- 600 Costa, A., Folch, A., and Macedonio, G.: A model for wet aggregation of ash particles in
601 volcanic plumes and clouds: 1. Theoretical formulation, *J. Geophys. Res.*, 115,
602 doi:10.1029/2009JB007175, 2010.

603 Dacre, H. F., Grant, A. L. M., Hogan, R. J., Belcher, S. E., Thomson, D. J., Devenish, B.,
604 Marengo, F., Haywood, J., Ansmann, A., and Mattis, I.: The structure and magnitude
605 of the ash plume during the initial phase of the Eyjafjallajökull eruption, evaluated
606 using lidar observations and NAME simulations, *J. Geophys. Res.*, 116, D00U03,
607 10.1029/2011JD015608, 2011.

608 Dartayat, M.: Observacion de la lluvia de cenizas del 11 de abril de 1932 en La Plata, *Revista*
609 *astronómica.*, 4, 183-187, 1932.

610 Degruyter, W., and Bonadonna, C.: Improving on mass flow rate estimates of volcanic
611 eruptions, *Geophys. Res. Lett.*, 39, L16308, 10.1029/2012GL052566, 2012.

612 Devenish, B., Francis, P. N., Johnson, B. T., Sparks, R. S. J., and Thomson, D. J.: Sensitivity
613 analysis of dispersion modeling of volcanic ash from Eyjafjallajökull in May 2010, *J.*
614 *Geophys. Res.*, 117, doi:10.1029/2011JD016782, doi:10.1029/2011JD016782, 2012.

615 Durant, A., and Rose, W. I.: Sedimentological constraints on hydrometeor-enhanced particle
616 deposition: 1992 eruptions of Crater Peak, Alaska, *J. Volcanol. Geotherm. Res.*, 186,
617 40-59, 2009.

618 Durant, A. J., Rose, W. I., Sarna-Wojcicki, A. M., Carey, S., and Volentik, A. C.:
619 Hydrometeor-enhanced tephra sedimentation: Constraints from the 18 May 1980
620 eruption of Mount St. Helens (USA), *J. Geophys. Res.*, 114,
621 doi:10.1029/2008JB005756, 2009.

622 Durant, A. J.: RESEARCH FOCUS: Toward a realistic formulation of fine-ash lifetime in
623 volcanic clouds, *Geology*, 43, 271-272, 10.1130/focus032015.1, 2015.

624 Eichelberger, J. C., Keith, T. E. C., Miller, T. P., and Nye, C. J.: The 1992 eruptions of Crater
625 Peak vent, Mount Spurr Volcano, Alaska: Chronology and summary, in: *The 1992*
626 *Eruptions of Crater Peak Vent, Mount Spurr Volcano, Alaska.* U.S. Geological
627 Survey Bulletin 2139, edited by: Keith, T. E. C., U.S. Government Printing Office,
628 Washington, D.C., 1-18, 1995.

629 Eychenne, J., Cashman, K., Rust, A., and Durant, A.: Impact of the lateral blast on the spatial
630 pattern and grain size characteristics of the 18 May 1980 Mount St. Helens fallout
631 deposit, *Journal of Geophysical Research: Solid Earth*, 120, 6018-6038,
632 10.1002/2015JB012116, 2015.

633 Fierstein, J., and Nathenson, M.: Another look at the calculation of fallout tephra volumes,
634 *Bull. Volcanol.*, 54, 156-167, 1992.

635 Folch, A., Costa, A., Durant, A., and Macedonio, G.: A model for wet aggregation of ash
636 particles in volcanic plumes and clouds: 2. Model application, *J. Geophys. Res.*, 115,
637 B09202, 10.1029/2009jb007176, 2010.

638 Foxworthy, B. L., and Hill, M.: Volcanic eruptions of 1980 at Mount St. Helens: The first 100
639 days. USGS Prof. Paper 1249, U.S. Government Printing Office, Washington, D.C.,
640 1982.

641 Gardner, C. A., Cashman, K. V., and Neal, C. A.: Tephra-fall deposits from the 1992 eruption
642 of Crater Peak, Alaska: implications of clast textures for eruptive processes, *Bull.*
643 *Volcanol.*, 59, 537-555, 1998.

644 Genareau, K., Proussevitch, A. A., Durant, A. J., Mulukutla, G., and Sahagian, D. L.: Sizing
645 up the bubbles that produce very fine ash during explosive volcanic eruptions,
646 *Geophys. Res. Lett.*, 39, L15306, 10.1029/2012GL052471, 2012.

647 Gilbert, J. S., and Lane, S. J.: The origin of accretionary lapilli, *Bull. Volcanol.*, 56, 398-411,
648 1994.

649 Harris, D. M., Rose, W. I., Roe, R., and Thompson, M. R.: Radar observations of ash
650 eruptions, in: *The 1980 Eruptions of Mount St. Helens*, Washington, edited by:

651 Lipman, P. W., and Mullineaux, D. R., U.S. Government Printing Office, Washington,
652 D.C., 323-333, 1981.

653 Hewett, T. A., Fay, J. A., and Hoult, D. P.: Laboratory experiments of smokestack plumes in
654 a stable atmosphere, *Atmospheric Environment*, 5, 767-789, 1971.

655 Holasek, R. E., and Self, S.: GOES weather satellite observations and measurements of the
656 May 18, 1980, Mount St. Helens eruption, *J. Geophys. Res.*, 100, 8469-8487, 1995.

657 Houghton, B. F., White, J. D. L., and Van Eaton, A. R.: Phreatomagmatic and Related
658 Eruption Styles, in: *The Encyclopedia of Volcanoes*, edited by: Sigurdsson, H.,
659 Houghton, B. F., Rymer, H., Stix, J., and McNutt, S. R., Elsevier, Amsterdam, 537-
660 552, 2015.

661 Hoult, D. P., and Weil, J. C.: Turbulent plume in a laminar cross flow, *Atmospheric
662 Environment*, 6, 513-531, 1972.

663 Hurst, A. W., and Turner, J. S.: Performance of the program ASHFALL for forecasting
664 ashfall during the 1995 and 1996 eruptions of Ruapehu volcano, *New Zealand Journal
665 of Geology and Geophysics*, 42, 615-622, 1999.

666 James, M. R., Gilbert, J. S., and Lane, S. J.: Experimental investigation of volcanic particle
667 aggregation in the absence of a liquid phase, *J. Geophys. Res.*, 107,
668 doi:10.1029/2001JB000950, 2002.

669 Kalnay, E., Kanamitsu, M., Kistler, R., Collins, W., Deaven, D., Gandin, L., Iredell, M., Saha,
670 S., White, G., Woollen, J., Zhu, Y., Leetmaa, A., Reynolds, R., Chelliah, M.,
671 Ebisuzaki, W., Higgins, W., Janowiak, J., Mo, K. C., Ropelewski, C., Wang, J., Jenne,
672 R., and Joseph, D.: The NCEP/NCAR 40-Year Reanalysis Project, *Bulletin of the
673 American Meteorological Society*, 77, 437-471, 10.1175/1520-
674 0477(1996)077<0437:TNYRP>2.0.CO;2, 1996.

675 Klawonn, M., Frazer, L. N., Wolfe, C. J., Houghton, B. F., and Rosenberg, M. D.:
676 Constraining particle size-dependent plume sedimentation from the 17 June 1996
677 eruption of Ruapehu Volcano, New Zealand, using geophysical inversions, *Journal of
678 Geophysical Research: Solid Earth*, 119, 1749-1763, 10.1002/2013JB010387, 2014.

679 Liu, J., Salmond, J. A., Dirks, K. N., and Lindsay, J. M.: Validation of ash cloud modelling
680 with satellite retrievals: a case study of the 16–17 June 1996 Mount Ruapehu eruption,
681 *Natural Hazards*, 10.1007/s11069-015-1753-3, 2015.

682 Macedonio, G., Pareschi, M. T., and Santacroce, R.: A Numerical Simulation of the Plinian
683 Fall Phase of 79 A.D. Eruption of Vesuvius, *J. Geophys. Res.*, 93, 14817-14827, 1988.

684 Manzella, I., Bonadonna, C., Phillips, J. C., and Monnard, H.: The role of gravitational
685 instabilities in deposition of volcanic ash, *Geology*, 43, 211-214, 10.1130/g36252.1,
686 2015.

687 Mastin, L. G., Guffanti, M., Servranckx, R., Webley, P., Barsotti, S., Dean, K., Denlinger, R.,
688 Durant, A., Ewert, J. W., Neri, A., Rose, W. I., Schneider, D., Siebert, L., Stunder, B.,
689 Swanson, G., Tupper, A., Volentik, A., and Waythomas, C. F.: A multidisciplinary
690 effort to assign realistic source parameters to models of volcanic ash-cloud transport
691 and dispersion during eruptions, *J. Volcanol. Geotherm. Res.*, 186, 10-21, 2009.

692 Mastin, L. G., Randall, M., J., Schwaiger, H., and Denlinger, R.: User's Guide and Reference
693 to Ash3d: A Three-Dimensional Model for Atmospheric Tephra Transport and
694 Deposition, in: *U.S. Geological Survey Open-File Report 2013-1122*, 48, 2013a.

695 Mastin, L. G., Schwaiger, H., Schneider, D. J., Wallace, K. L., Schaefer, J., and Denlinger, R.
696 P.: Injection, transport, and deposition of tephra during event 5 at Redoubt Volcano,
697 23 March, 2009, *J. Volcanol. Geotherm. Res.*, 259, 201-213,
698 <http://dx.doi.org/10.1016/j.jvolgeores.2012.04.025>, 2013b.

699 Mastin, L. G.: Testing the accuracy of a 1-D volcanic plume model in estimating mass
700 eruption rate, *Journal of Geophysical Research: Atmospheres*, 119, 2013JD020604,
701 10.1002/2013JD020604, 2014.

702 McGimsey, R. G., Neal, C. A., and Riley, C.: Areal distribution, thickness, volume, and grain
703 size of tephra-fall deposits from the 1992 eruptions of Crater Peak vent, Mt. Spurr
704 volcano, Alaska, in: U.S. Geological Survey Open-File Report 01-0370, U.S.
705 Government Printing Office, Washington, D.C., 38, 2001.

706 Mesinger, F., DiMego, G., Kalnay, E., Mitchell, K., Shafran, P. C., Ebisuzaki, W., Jovic, D.,
707 Woollen, J., Rogers, E., Berbery, E. H., Ek, M. B., Fan, Y., Grumbine, R., Higgins,
708 W., Li, H., Lin, Y., Manikin, G., Parrish, D., and Shi, W.: North American Regional
709 Reanalysis, *Bulletin of the American Meteorological Society*, 87, 343-360,
710 DOI:10.1175/BAMS-87-3-343, 2006.

711 Nakagawa, M., Wada, K., Thordarson, T., Wood, C. P., and Gamble, J. A.: Petrologic
712 investigations of the 1995 and 1996 eruptions of Ruapehu volcano, New Zealand:
713 Formation of discrete and small magma pockets and their intermittent discharge, *Bull.*
714 *Volcanol.*, 61, 15-31, 1999.

715 Neal, C. A., McGimsey, R. G., Gardner, C. A., Harbin, M., L., and Nye, C. J.: Tephra-fall
716 deposits from the 1992 eruptions of Crater Peak, Mount Spurr, Alaska, in: *The 1992*
717 *eruptions of Crater Peak, Mount Spurr, Alaska*, U.S.G.S. Bulletin 2139, edited by:
718 Keith, T. E. C., U.S. Geological Survey, Washington, D.C., 65-79, 1995.

719 Prata, A. J., and Grant, I. F.: Retrieval of microphysical and morphological properties of
720 volcanic ash plumes from satellite data: application to Mt. Ruapehu, New Zealand,
721 *Quarterly Journal of the Royal Meteorological Society*, 127, 2153-2179, 2001.

722 Pyle, D. M.: The thickness, volume and grain size of tephra fall deposits, *Bull. Volcanol.*, 51,
723 1-15, 1989.

724 Rice, C. J.: Satellite observations of the Mt. St. Helens eruption of 18 May 1980, in:
725 *Technical Report, Aerosp. Corp., Space Sci. Lab., El Segundo, CA*, 1981.

726 Rose, W. I., Delene, D. J., Schneider, D. J., Bluth, G. J. S., Krueger, A. J., Sprod, I., McKee,
727 C., Davies, H. L., and Ernst, G. G. J.: Ice in the 1994 Rabaul eruption cloud:
728 implications for volcano hazard and atmospheric effects, *Nature*, 375, 477-479, 1995a.

729 Rose, W. I., Kostinski, A. B., and Kelley, L.: Real-time C-band radar observations of th 1992
730 eruption clouds from Crater Peak, Mount Spurr Volcano, Alaska, in: *The 1992*
731 *Eruptions of Crater Peak Vent, Mount Spurr Volcano, Alaska*. U.S. Geological
732 Survey Bulletin 2139, edited by: Keith, T. E. C., U.S. Government Printing Office,
733 Washington. D.C., 19-26, 1995b.

734 Rose, W. I., and Durant, A.: Fine ash content of explosive eruptions, *J. Volcanol. Geotherm.*
735 *Res.*, 186, 32-39, 2009.

736 Rosenbaum, J., and Waitt, R.: A summary of eyewitness accounts of the May 18 eruption, in:
737 *The 1980 eruptions of Mount St. Helens*, Washington, edited by: Lipman, P. W., and
738 Mullineaux, D. R., U.S. Government Printing Office, Washington, D.C., 53-67, 1981.

739 Rutherford, M. J., Sigurdsson, H., Carey, S., and Davis, A.: The May 18, 1980, eruption of
740 Mount St. Helens: 1, Melt composition and experimental phase equilibria, *J. Geophys.*
741 *Res.*, 90, 2929-2947, 1985.

742 Sarna-Wojcicki, A. M., Shipley, S., Waitt, R., Dzurisin, D., and Wood, S. H.: Areal
743 distribution, thickness, mass, volume, and grain size of air-fall ash from the six major
744 eruptions of 1980, in: *The 1980 Eruptions of Mount St. Helens*, Washington; U.S.
745 Geological Survey Professional Paper 1250, edited by: Lipman, P. W., and
746 Christiansen, R. L., U.S. Geological Survey, 577-601, 1981.

- 747 Schneider, D. J., and Hoblitt, R. P.: Doppler weather radar observations of the 2009 eruption
748 of Redoubt Volcano, Alaska, *J. Volcanol. Geotherm. Res.*, 259, 133-144, 2013.
- 749 Schultz, D. M., Kanak, K. M., Straka, J. M., Trapp, R. J., Gordon, B. A., Zrnić, D. S., Bryan,
750 G. H., Durant, A. J., Garrett, T. J., Klein, P. M., and Lilly, D. K.: The Mysteries of
751 Mammatus Clouds: Observations and Formation Mechanisms, *Journal of the*
752 *Atmospheric Sciences*, 63, 2409-2435, 10.1175/JAS3758.1, 2006.
- 753 Schumacher, R., and Schmincke, H. U.: Internal structure and occurrence of accretionary
754 lapilli - a case study at Laacher See Volcano, *Bull. Volcanol.*, 53, 612-634, 1991.
- 755 Schumacher, R., and Schmincke, H. U.: Models for the origin of accretionary lapilli, *Bull.*
756 *Volcanol.*, 56, 626-639, DOI: 10.1007/s004450050069 1995.
- 757 Schwaiger, H., Denlinger, R., and Mastin, L. G.: Ash3d: a finite-volume, conservative
758 numerical model for ash transport and tephra deposition, *J. Geophys. Res.*, 117,
759 doi:10.1029/2011JB008968, doi:10.1029/2011JB008968, 2012.
- 760 Scollo, S., Tarantola, S., Bonadonna, C., Coltelli, M., and Saltelli, A.: Sensitivity analysis and
761 uncertainty estimation for tephra dispersal models, *J. Geophys. Res.*, 113,
762 doi:10.1029/2006JB004864, doi:10.1029/2006JB004864, 2008.
- 763 Sisson, T. W.: Blast ashfall deposit of May 18, 1980 at Mount St. Helens, Washington, *J.*
764 *Volcanol. Geotherm. Res.*, 66, 203-216, 1995.
- 765 Sorem, R. K.: Volcanic ash clusters: Tephra rafts and scavengers, *J. Volcanol. Geotherm.*
766 *Res.*, 13, 63-71, 1982.
- 767 Suzuki, T.: A Theoretical model for dispersion of tephra, in: *Arc Volcanism: Physics and*
768 *Tectonics*, edited by: Shimozuru, D., and Yokoyama, I., Terra Scientific Publishing
769 Company, Tokyo, 95-113, 1983.
- 770 Swanson, D. A., Weaver, S. J., and Houghton, B. F.: Reconstructing the deadly eruptive
771 events of 1790 CE at Kīlauea Volcano, Hawai‘i, *Geological Society of America*
772 *Bulletin*, 10.1130/b31116.1, 2014.
- 773 Taddeucci, J., Scarlato, P., Montanaro, C., Cimarelli, C., Del Bello, E., Freda, C., Andronico,
774 D., Gudmundsson, M. T., and Dingwell, D. B.: Aggregation-dominated ash settling
775 from the Eyjafjallajökull volcanic cloud illuminated by field and laboratory high-speed
776 imaging, *Geology*, 39, 891-894, 10.1130/g32016.1, 2011.
- 777 Van Eaton, A. R., Muirhead, J. D., Wilson, C. J. N., and Cimarelli, C.: Growth of volcanic
778 ash aggregates in the presence of liquid water and ice: an experimental approach, *Bull.*
779 *Volcanol.*, 74, 1963-1984, 10.1007/s00445-012-0634-9, 2012.
- 780 Van Eaton, A. R., and Wilson, C. J. N.: The nature, origins and distribution of ash aggregates
781 in a large-scale wet eruption deposit: Oruanui, New Zealand, *J. Volcanol. Geotherm.*
782 *Res.*, 250, 129-154, 2013.
- 783 Van Eaton, A. R., Mastin, L. G., Herzog, M., Schwaiger, H. F., Schneider, D. J., Wallace, K.
784 L., and Clarke, A. B.: Hail formation triggers rapid ash aggregation in volcanic
785 plumes, *Nat Commun*, 6, 10.1038/ncomms8860, 2015.
- 786 Van Eaton, A. R., Mastin, L. G., Herzog, M., Schwaiger, H., Schneider, D., Wallace, D. A.,
787 and Clarke, A.: Hail formation as a mechanism of rapid ash aggregation in volcanic
788 clouds, *Nature Communications*, in press.
- 789 Waitt, R.: Devastating pyroclastic density flow and attendant air fall of May 18 - Stratigraphy
790 and sedimentology of deposits, in: *The 1980 Eruptions of Mount St. Helens,*
791 *Washington. U.S. Geological Survey Professional Paper 1250*, edited by: Lipman, P.
792 W., and Mullineaux, D. R., U.S. Government Printing Office, Washington, D.C., 438-
793 458, 1981.
- 794 Waitt, R., and Dzurisin, D.: proximal air-fall deposits from the May 18 eruption--stratigraphy
795 and field sedimentology, in: *The 1980 Eruptions of Mount St. Helens, Washington,*

796 edited by: Lipman, P. W., and Mullineaux, D. R., U.S. Geological Survey Professional
797 Paper 1250, U.S. Government Printing Office, Washington, D.C., 601-615, 1981.
798 Wallace, K. L., Schaefer, J. R., and Coombs, M. L.: Character, mass, distribution, and origin
799 of tephra-fall deposits from the 2009 eruption of Redoubt Volcano, Alaska—
800 Highlighting the significance of particle aggregation, *J. Volcanol. Geotherm. Res.*,
801 259, 145-169, <http://dx.doi.org/10.1016/j.jvolgeores.2012.09.015>, 2013.
802 Wen, S., and Rose, W. I.: Retrieval of sizes and total masses of particles in volcanic clouds
803 using AVHRR bands 4 and 5, *J. Geophys. Res.*, 99, 5421-5431, 1994.
804 Wilson, L., and Huang, T. C.: The influence of shape on the atmospheric settling velocity of
805 volcanic ash particles, *Earth Planet. Sci. Lett.*, 44, 311-324, 1979.
806 Woodhouse, M. J., Hogg, A. J., Phillips, J. C., and Sparks, R. S. J.: Interaction between
807 volcanic plumes and wind during the 2010 Eyjafjallajökull eruption, Iceland, *Journal*
808 *of Geophysical Research: Solid Earth*, 118, 92-109, 10.1029/2012JB009592, 2013.
809

810 **Tables**

811 Table 1: Input parameters for simulations. Vent elevation is given in kilometers above mean
 812 sea level.

| PARAMETER(S) | MOUNT ST. HELENS | SPURR | RUAPEHU | REDOUBT |
|---|-------------------------------------|---|---|-------------------------------------|
| MODEL DOMAIN | 42-49°N 124-110°W 0-35 km asl | 59-64°N 155.6- 141.4°W 0-17 km asl | 39.5-37.5°S 175-177°E 0-12 km asl | 60-64°N 155-145°W 0-20 km asl |
| VENT LOCATION | 122.18°W 46.2°N | 152.25°W 61.23°N | 175.56°E 39.28°S | 152.75°W 60.48°N |
| VENT ELEVATION (KM) | 2.00 | 2.30 | 2.80 | 2.30 |
| NODAL SPACING | 0.1° horizontal 1.0 km vertical | 0.1° horizontal 1.0 km vertical | 0.025° horizontal 0.5 km vertical | 0.07° horizontal 1.0 km vertical |
| ERUPTION START DATE (UTC) (YYYY.MM.DD) | 1980.05.18 | 1992.09.17 | 1996.06.16 1996.06.17 | 2009.03.23 |
| START TIME (UTC) | 1530 UTC | 0803 UTC | 2030 UTC 0200 UTC | 1230 UTC |
| PLUME HEIGHT, KM ASL | See Table 2 | 13 | 8.5 | 15 |
| DURATION, HRS | See Table 2 | 3.6 | 4.5 2.0 | 0.33 |
| ERUPTED VOLUME KM ³ DRE | 0.2 (total) | 0.014 | 0.000643 0.000357 | 0.0017 |
| DIFFUSION COEFFICIENT <i>D</i> | 0 | 0 | 0 | 0 |
| SUZUKI CONSTANT <i>K</i> | 8 | 8 | 8 | 8 |
| PARTICLE SHAPE FACTOR <i>F</i> | 0.44 | 0.44 | 0.44 | 0.44 |
| AGGREGATE SHAPE FACTOR <i>F</i> | 1.0 | 1.0 | 1.0 | 1.0 |

813

814

815 Table 2: Time series of plume height and total erupted volume used in model simulations of
 816 the Mount St. Helens ash cloud. H =plume height in km above sea level (a.s.l.), V =erupted
 817 volume in million cubic meters dense-rock equivalent (DRE). The time series of plume height
 818 approximates that measured by radar (Harris et al., 1981). We calculated a preliminary eruptive
 819 volume for each eruptive pulse using the duration and the empirical relationship between plume
 820 height and eruption rate (Mastin et al., 2009). This method underestimated the eruptive volume,
 821 as noted in previous studies (Carey et al., 1990). Hence we adjusted the volume of each pulse
 822 proportionately so that their total equals the 0.2 km³ DRE estimated by Sarna-Wojcicki et al.
 823 (1981). For the last two eruptive pulses, start times in UTC, marked with asterisks, are on 19
 824 May in UTC time. All other start times are on 18 May.

Plume height (H), duration (D) and volume (V)

| start | | D | H | V |
|-------|-------|------------|---------------|----------------------------------|
| PDT | UTC | <i>min</i> | <i>km asl</i> | $\times 10^6$ m ³ DRE |
| 8:30 | 1530 | 30 | 25 | 3.247 |
| 9:00 | 1600 | 36 | 15.3 | 0.077 |
| 9:36 | 1636 | 54 | 13.7 | 0.356 |
| 10:30 | 1730 | 45 | 15.3 | 0.502 |
| 11:15 | 1815 | 30 | 16.1 | 0.426 |
| 11:45 | 1845 | 42 | 17.4 | 0.615 |
| 12:27 | 1927 | 48 | 17.4 | 0.615 |
| 13:15 | 2015 | 60 | 14.6 | 0.183 |
| 14:15 | 2115 | 45 | 14.7 | 0.535 |
| 15:30 | 2230 | 60 | 15.8 | 0.691 |
| 16:30 | 2330 | 60 | 19.2 | 0.700 |
| 17:30 | 0030* | 60 | 7.7 | 1.945 |
| 18:30 | 0130* | 60 | 6.2 | 0.020 |

825

826 Table 3. Statistical measures of fit used in this paper

| Name | Formula | Explanation |
|---------------------------------|--|--|
| Point-by-point method | $\Delta^2 = \left[\frac{\sum_{i=1}^N (m_{m,i} - m_{o,i})^2}{\sum_{i=1}^N m_{o,i}^2} \right]$ | <p>The mass load $m_{o,i}$ observed at each sample location i is compared with modeled mass load $m_{m,i}$ at the same location. Squared differences are summed to the total number of sample points N, and normalized to the sum of squares of the observed mass loads.</p> |
| Downwind thinning method | $\Delta_{downwind}^2 = \frac{1}{M} \sum_{j=1}^M (\log(m_{m,j} / m_{o,j}))^2$ | <p>The log of modeled mass load $m_{m,j}$ at a point j on the dispersal axis, is compared with the observation-based value $m_{o,j}$ expected at that location based on a trend line drawn between field measurements along the axis (Fig. 4). Differences between $m_{m,j}$ and $m_{o,j}$ are calculated on a log scale, squared, and summed.</p> |
| Isomass area method | $\Delta_{area}^2 = \left[\frac{\sum_{i=1}^L (A_{m,i} - A_{o,i})^2}{\sum_{i=1}^L A_{o,i}^2} \right]$ | <p>This method calculates the area $A_{m,i}$ of the modeled deposit that exceeds a given mass load i by summing the area of all model nodes that meet this criterion. It then takes the difference between $A_{m,i}$ and the area $A_{o,i}$ within same isomass line mapped from field observations. The sum of the squares of these differences, normalized to the sum of the squared mapped isopach areas, gives the index Δ_{area}^2.</p> |

827
828
829

830 Table 4: percentage of fine ash assigned to different size bins for different values of σ_{agg} . The
 831 mass fraction m_ϕ in each bin (ϕ) was calculated using the equation for a Poisson distribution,
 832 $m_\phi = (1/\sqrt{2\pi}) \exp\left\{-\left(\phi - \mu_{agg}\right)^2 / (2\sigma_{agg})^2\right\}$. Values of m_ϕ were then adjusted proportionally
 833 so that their sum added to 1.

| Bin | $\sigma_{agg}=0$ | 0.1 | 0.2 | 0.3 |
|-----------------------|------------------|-----|-----|------|
| $\mu_{agg} - 0.6\phi$ | | | | 1.9 |
| $\mu_{agg} - 0.5\phi$ | | | 0.9 | 3.4 |
| $\mu_{agg} - 0.4\phi$ | | | 2.7 | 5.6 |
| $\mu_{agg} - 0.3\phi$ | | | 6.5 | 8.3 |
| $\mu_{agg} - 0.2\phi$ | | 6 | 12 | 11.0 |
| $\mu_{agg} - 0.1\phi$ | | 24 | 18 | 13.0 |
| μ_{agg} | 100 | 40 | 20 | 13.7 |
| $\mu_{agg} + 0.1\phi$ | | 24 | 18 | 13.0 |
| $\mu_{agg} + 0.2\phi$ | | 6 | 12 | 11.0 |
| $\mu_{agg} + 0.3\phi$ | | | 6.5 | 8.3 |
| $\mu_{agg} + 0.4\phi$ | | | 2.7 | 5.6 |
| $\mu_{agg} + 0.5\phi$ | | | 0.9 | 3.4 |
| $\mu_{agg} + 0.6\phi$ | | | | 1.9 |

834

835

836 Table 5: Atmospheric temperature profiles during the eruptions at Mount St. Helens, Crater
837 Peak (Spurr), Ruapehu, and Redoubt volcanoes. Profile for Mount St. Helens is for 18 May
838 1980, 1800 UTC, interpolated to the location of Ritzville, Washington (47.12°N, 118.38°W).
839 For Crater Peak (Spurr) the profile is for 17 September 1992, 1200 UTC, interpolated to the
840 location of Palmer, Alaska (61.6°N, 149.11°W). For Ruapehu the temperature profile is for
841 17 June 1996, 0000 UTC, interpolated to the location of Ruapehu. For Redoubt the sounding
842 was for 23 March 2009, 1200 UTC, at 62°N, 153°W. All soundings were taken from RE1
843 reanalysis data available at <http://ready.arl.noaa.gov/READYamet.php>. For Mount St.
844 Helens, the freezing elevation was also checked using data from the North American Regional
845 Reanalysis (NARR) model (Mesinger et al., 2006), available at the same NOAA site, and
846 found to be 3.3 km, similar to that given below by the RE1 model.
847

| p (hPa) | <i>Mount St. Helens</i> | | <i>Crater Peak (Spurr)</i> | | <i>Ruapehu</i> | | <i>Redoubt</i> | |
|---------|-------------------------|-------|----------------------------|-------|----------------|-------|----------------|-------|
| | z (m) | T (C) | z (m) | T (C) | z (m) | T (C) | z (m) | T (C) |
| 10 | 31,381 | -39.9 | 31,137 | -41.8 | 30,632 | -54.9 | 30,179 | -61.9 |
| 20 | 26,713 | -47.5 | 26,535 | -51.0 | 26,239 | -57.9 | 25,891 | -62.1 |
| 30 | 24,067 | -52.1 | 23,920 | -54.4 | 23,673 | -56.6 | 23,385 | -61.3 |
| 50 | 20,786 | -55.7 | 20,660 | -55.5 | 20,441 | -57.1 | 20,185 | -57.6 |
| 70 | 18,646 | -55.8 | 18,515 | -55.6 | 18,307 | -56.4 | 18,049 | -55.1 |
| 100 | 16,377 | -55.4 | 16,241 | -55.3 | 16,041 | -56 | 15,759 | -53.1 |
| 150 | 13,782 | -55.1 | 13,646 | -56.0 | 13,439 | -54.2 | 13,133 | -51 |
| 200 | 11,962 | -58.3 | 11,833 | -58.9 | 11,613 | -58.6 | 11,255 | -50.4 |
| 250 | 10,552 | -53.4 | 10,412 | -51.3 | 10,214 | -58.3 | 9,814 | -54.7 |
| 300 | 9,355 | -44 | 9,200 | -41.0 | 9,057 | -53.4 | 8,652 | -55.5 |
| 400 | 7,355 | -28.5 | 7,174 | -25.0 | 7,151 | -38.9 | 6,764 | -41.9 |
| 500 | 5,716 | -16.4 | 5,519 | -15.5 | 5,576 | -26.7 | 5,225 | -33.9 |
| 600 | 4,318 | -6.9 | 4,126 | -10.2 | 4,231 | -15.5 | 3,929 | -27.4 |
| 700 | 3,100 | 0.1 | 2,929 | -6.7 | 3,049 | -8.6 | 2,802 | -19.5 |
| 850 | 1,515 | 10.3 | 1,397 | -2.0 | 1,524 | -1.4 | 1,330 | -9.7 |
| 925 | -- | -- | 722 | -0.2 | 844 | 3.8 | 675 | -8.9 |

848

849

850 **Figure captions**

851 Figure 1: Maps of the deposits investigated in this work: (a) Mount St. Helens, 18 May 1980;
852 (b) Crater Peak, 16-17 September, 1992; (c) Ruapehu, 17 June, 1996; and (d) Redoubt, 23
853 March, 2009. Isomass lines for Mount St. Helens were digitized from Fig. 438 in Sarna-
854 Wojcicki et al. (1981); for Crater Peak from Fig. 16 in McGimsey et al. (2001); for Ruapehu
855 from Fig. 1 of Bonadonna and Houghton (2005); and for Redoubt from Wallace et al. (2013).
856 Isomass values are all in kg m^{-2} . Colored markers represent locations where isomass was
857 sampled, with colors corresponding to the mass load shown in the color table. Black dashed
858 lines indicate the dispersal axis. Sample locations for Mount St. Helens taken from
859 supplementary material in Durant et al. (2009); for Redoubt from Wallace et al. (2013), for
860 Crater Peak from McGimsey et al. (2001) and for Ruapehu, from data posted online at the
861 IAVCEI Commission on Tephra Hazard Modeling database (<http://dbstr.ct.ingv.it/iavcei/>
862 (Bonadonna and Houghton, 2005; Bonadonna et al., 2005)).

863 Figure 2: Illustration of the path taken by coarse aggregates that fallout in proximal sections,
864 less than a few plume heights from the source (left), and fine aggregates that fall out in distal
865 sections (right). Among distal fine aggregates, we show the path taken by those that might have
866 formed within or below the downwind cloud as hypothesized by Durant et al. (2009) (red
867 dashed line), and those that were transported downwind without changing size, as calculated
868 by Ash3d (blue dashed line). Also illustrated are some key processes that might influence the
869 distribution of fine, distal ash, including development of gravitational instability and overturn
870 within the downwind cloud (Carazzo and Jellinek, 2012), and the development of
871 hydrometeors as descending ash approaches the freezing elevation (Durant et al., 2009).

872 Figure 3: Total particle size distribution for each of the deposits studied: (a) Mount St. Helens,
873 (b) Crater Peak (Mount Spurr), (c) Ruapehu, and (d) Redoubt. Gray bars show the original
874 TPSD before aggregation. Black bars show the sizes not involved in aggregation; red bars show
875 sizes of aggregate classes used in Figs. 11-14.

876 Figure 4: Mass load versus downwind distance along the dispersal axis for the deposits of (a)
877 Mount St. Helens, (b) Crater Peak (Mount Spurr), (c) Ruapehu, and (d) Redoubt. Squares
878 indicate sample points within 20 km of the dispersal axis, with the grayscale value indicating
879 the distance from the dispersal axis following the color bar in (a). The dash trend lines represent

880 interpolated values of the mass load that are compared with modeled values to calculate
881 $\Delta_{downwind}^2$.

882 Figure 5: Log mass load versus the square root of the area within isomass lines mapped for the
883 (a) Mount St. Helens; (b) Crater Peak (Spurr); (c) Ruapehu; and (d) Redoubt deposits. Also
884 shown are best-fit lines, drawn by visual inspection, using either one line segment (Ruapehu,
885 Redoubt) or two, where justified (Spurr, St. Helens). Triangular markers are marked with labels
886 indicating the approximate percentage of the deposit mass lying inboard of these points, as
887 calculated using equations derived from Fierstein and Nathenson (1992).

888 Figure 6: (a) Transport distance versus average fall velocity, assuming a 15.1 m s^{-1} wind speed,
889 equal to the average wind speed at Mount St. Helens between 0 and 15 km, and a fall distance
890 of 15 km. The vertical shaded bar represents the distance of Ritzville. Labels on dots give the
891 average diameter of a round aggregate having a density of 600 kg m^{-3} and the given fall velocity.
892 (b) Average fall velocity between 0 and 15 km elevation, versus aggregate diameter, for round
893 aggregates having densities ranging from 200 to $2,500 \text{ kg m}^{-3}$. The horizontal shaded bar
894 represents the range of average fall velocities that would land in Ritzville. Fall velocities are
895 calculated using relations of Wilson and Huang (1979), at 1-km elevation intervals in the
896 atmosphere, from 0 to 15 km, then averaged to derive the values plotted.

897 Figure 7: Deposit maps for simulations using a single size class representing an aggregate with
898 ϕ size 1.9 and density 600 kg m^{-3} , using three shape factors: (a) $F=0.44$; (b) $F=0.7$; and (c)
899 $F=1.0$. Inset figures illustrate ellipsoids having the given shape factor, assuming $b=(a+c)/2$.

900 Figure 8: Deposit map for simulations using a single size class representing an aggregate with
901 $F=1.0$, ϕ size 2.4ϕ and density 600 kg m^{-3} . Figs. 8a, b, and c, illustrate the deposit distribution
902 using Suzuki k values of 4, 8, and 12, while Fig. 8d illustrates the deposit distribution resulting
903 from release of all the erupted mass from a single node at the top of the plume. Inset plots
904 schematically illustrate the vertical distribution of mass with height in the plume for each of
905 these cases. Simulations used other input values as given in Table 1. Colored dots represent
906 sample locations with colors indicating the sampled mass load, as in Fig. 1a.

907 Figure 9: Results of Mount St. Helens simulations using a single size class of round aggregates
908 in each simulation: $\phi=1.8, 2.0, 2.2, 2.4,$ and 2.6 in (a), (b), (c), (d), and (e); (f) shows the mapped
909 mass load, digitized from Fig. 438 in Sarna-Wojcicki et al. [1981]. Markers in each figure
910 provide the sample locations, with colors indicating the mass load measured at each location,

911 as shown in the color bar. Lines are contours of mass load with colors giving their values. The
912 mass load values of the contour lines, from lowest to highest, are 0.01, 0.1, 0.5, 1, 5, 10, 20, 30,
913 50, 80, and 100 kg m⁻² respectively.

914 Figure 10: Contours of Δ^2 (left column), $\Delta_{downwind}^2$ (middle column), and Δ_{area}^2 (right column)
915 as a function of σ_{agg} and μ_{agg} for deposits from Mount St. Helens (top row); Crater Peak (Mount
916 Spurr, second row); Ruapehu (third row), and Redoubt (bottom row). The values of these
917 contour lines are indicated by the color using the color bar at the right. Maximum and minimum
918 values in the color scale are given within each frame. The best agreement between model and
919 mapped data is indicated by the deep blue and purple contours; the worst is indicated by the
920 yellow contours. Regions of each plot where agreement is best is indicated by the word “Lo”.

921 Figure 11: Results of the Mount St. Helens simulation that provides approximately the best fit
922 to mapped data ($\mu_{agg}=2.4\phi$ and $\sigma_{agg}=0.1\phi$). (a) Deposit map with modeled isomass lines and
923 dots that represent field measurements with colors indicating the field values of the mass load,
924 corresponding to the color bar at left. The black dashed line indicates the dispersal axis of the
925 mapped deposit whereas the solid black line with dots indicates the dispersal axis of the
926 modeled deposit (the latter lies mostly on top of the former and obscures it). The modeled
927 dispersal axis was obtained by finding the ground cell in each column of longitude with the
928 highest deposit mass load. (b) Log of modeled mass load versus measured mass load at sample
929 locations. Black dashed line is the 1:1 line; dotted lines above and below indicate modeled
930 values 10 and 0.1 times that measured. Gray dots lay outside the range of downwind distances
931 covered by trend lines in Fig. 4 and therefore were not included in the calculation of Δ^2 . (c)
932 Log of measured mass load (black and gray dots), and modeled mass load (black line with dots)
933 versus distance downwind along the dispersal axis. The black dashed line is the same trend
934 line as in Fig. 4a. Gray dots were not included in the calculation of $\Delta_{downwind}^2$. (d) Log of mass
935 load versus square root of area contained within isomass lines. Black squares are from the
936 mapped deposit, red squares from the modeled one.

937 Figure 12: Results of the Crater Peak (Mount Spurr) simulation that provides a good fit to
938 mapped data ($\mu_{agg}=2.4\phi$ and $\sigma_{agg}=0.1\phi$). The features in the sub-figures are as described in Fig.
939 11. “CP” in Fig. 12a refers to the Crater Peak vent.

940 Figure 13: Results of the Ruapehu simulation that provides a good best fit to mapped data (μ_{agg}
941 $=2.4\phi$ and $\sigma_{agg}=0.1\phi$). The features in the sub-figures are as described in Fig. 11.

942 Figure 14: Results of the Redoubt simulation that provides a reasonable fit to mapped data (
943 $\mu_{agg}=2.4\phi$ and $\sigma_{agg}=0.1\phi$). The features in the sub-figures are as described in Fig. 11.

944 Figure 15: Modeled mass load of the Mount St. Helens eruption for four cases using $\mu_{agg}=2.4\phi$,
945 $\sigma_{agg}=0.1\phi$, and different diffusion coefficients: (a) $D=0 \text{ m}^2 \text{ s}^{-1}$, (b) $3\times 10^2 \text{ m}^2 \text{ s}^{-1}$, (c) $1\times 10^3 \text{ m}^2 \text{ s}^{-1}$,
946 and (d) $3\times 10^3 \text{ m}^2 \text{ s}^{-1}$. Other inputs are as given in Tables 1 and 2. Lines are isomass contours
947 of modeled mass load and colored dots are sample locations. Colors of the dots and lines give
948 the mass load corresponding to the color table.

949 Figure 16: Modeled mass load of the Ruapehu eruption for four cases using $\mu_{agg}=2.4\phi$, σ_{agg}
950 $=0.1\phi$, and different diffusion coefficients: (a) $D=0 \text{ m}^2 \text{ s}^{-1}$, (b) $1\times 10^2 \text{ m}^2 \text{ s}^{-1}$, (c) $3\times 10^2 \text{ m}^2 \text{ s}^{-1}$,
951 and (d) $1\times 10^3 \text{ m}^2 \text{ s}^{-1}$. Other inputs are as given in Table 1. Lines are isomass contours of
952 modeled mass load and colored dots are sample locations. Colors of the dots and lines give the
953 mass load corresponding to the color table.

954 Figures S001-S004: Figures analogous to Figs. 11, 12, 13, and 14, respectively, but with no
955 particle aggregation.

956 Figures S005-S056: Figures analogous to Fig. 11, but for different values of μ_{agg} and σ_{agg}
957 given in their labels.

958 Figures S057-S108: Figures analogous to Fig. 12, but for different values of μ_{agg} and σ_{agg} given
959 in their labels.

960 Figures S109-S160: Figures analogous to Fig. 13, but for different values of μ_{agg} and σ_{agg} given
961 in their labels.

962 Figures S161-S212: Figures analogous to Fig. 14, but for different values of μ_{agg} and σ_{agg} given
963 in their labels.

964

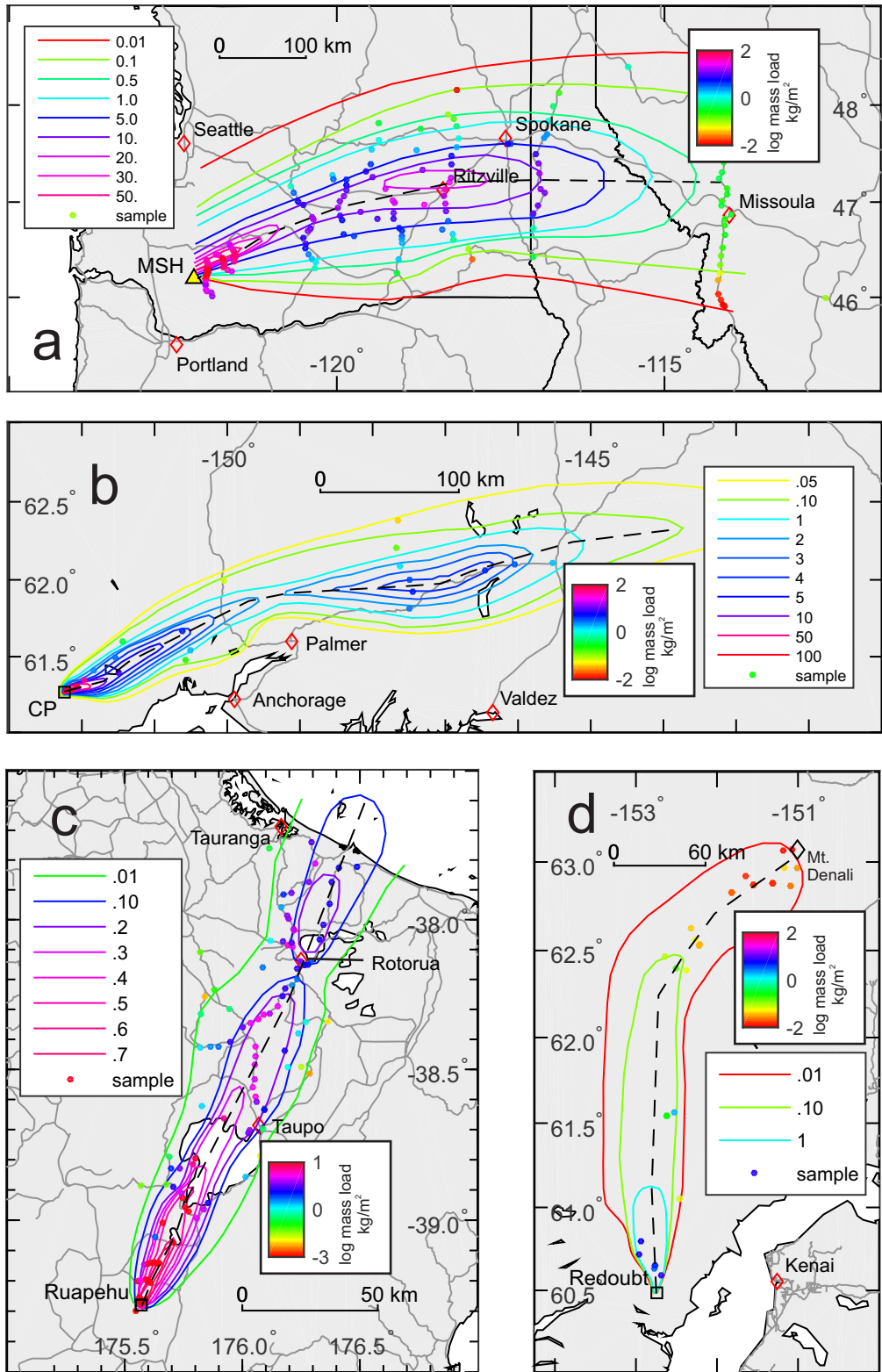


Figure 1

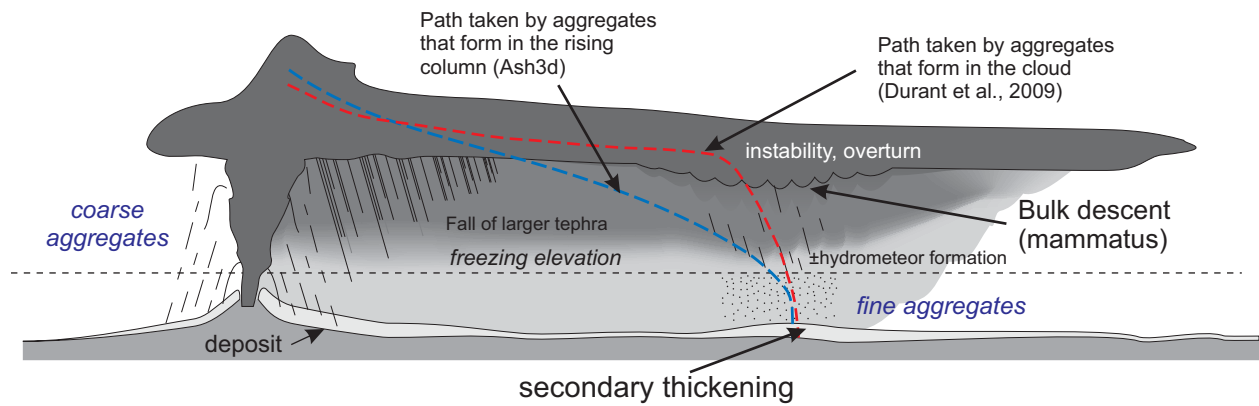


Figure 2

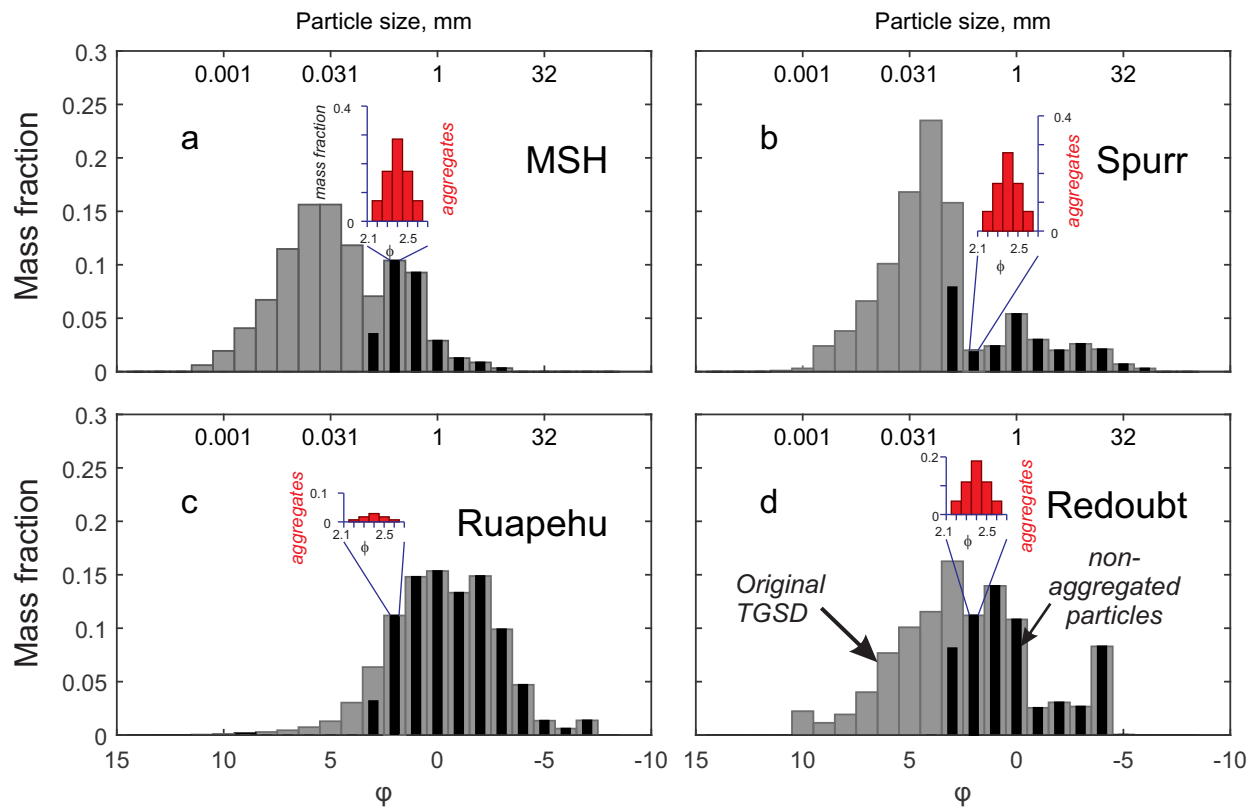


Figure 3

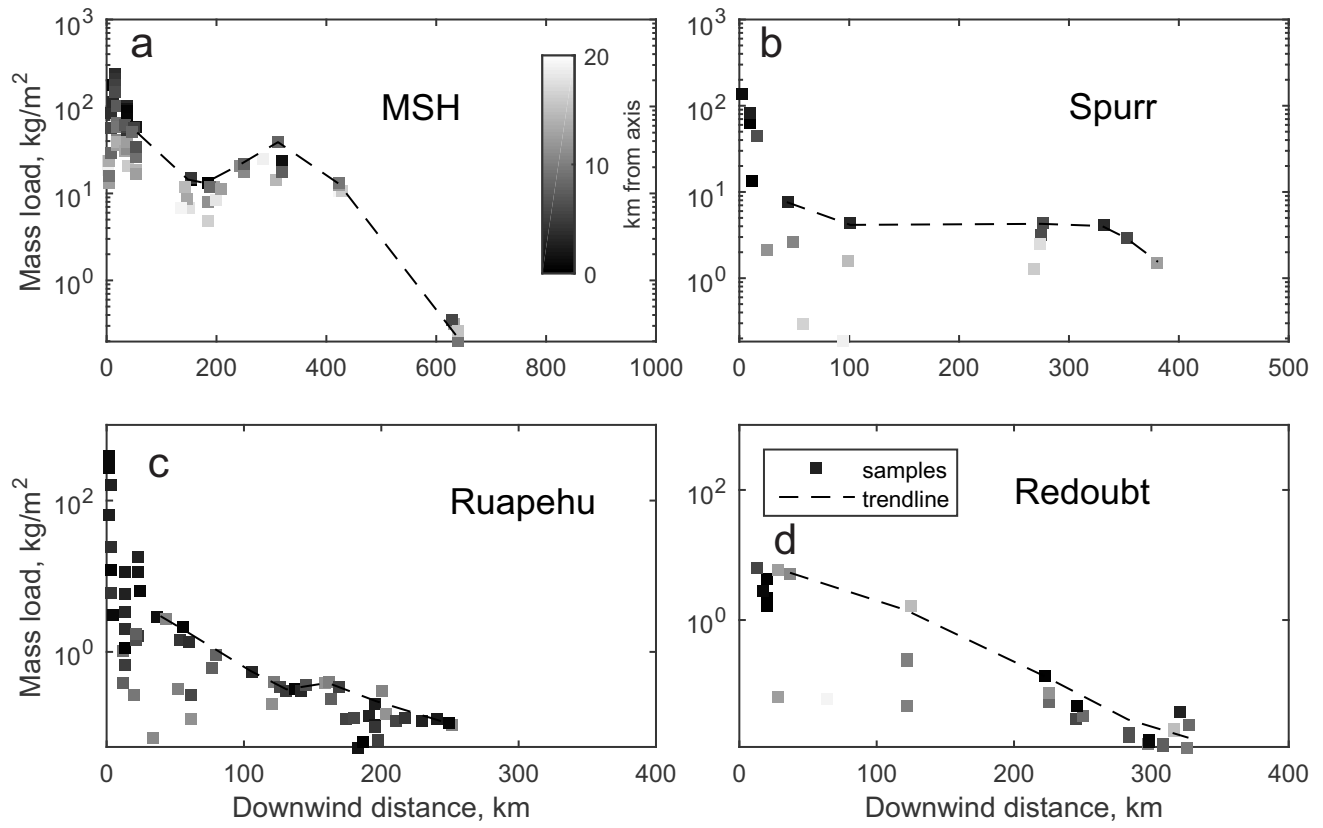


Figure 4

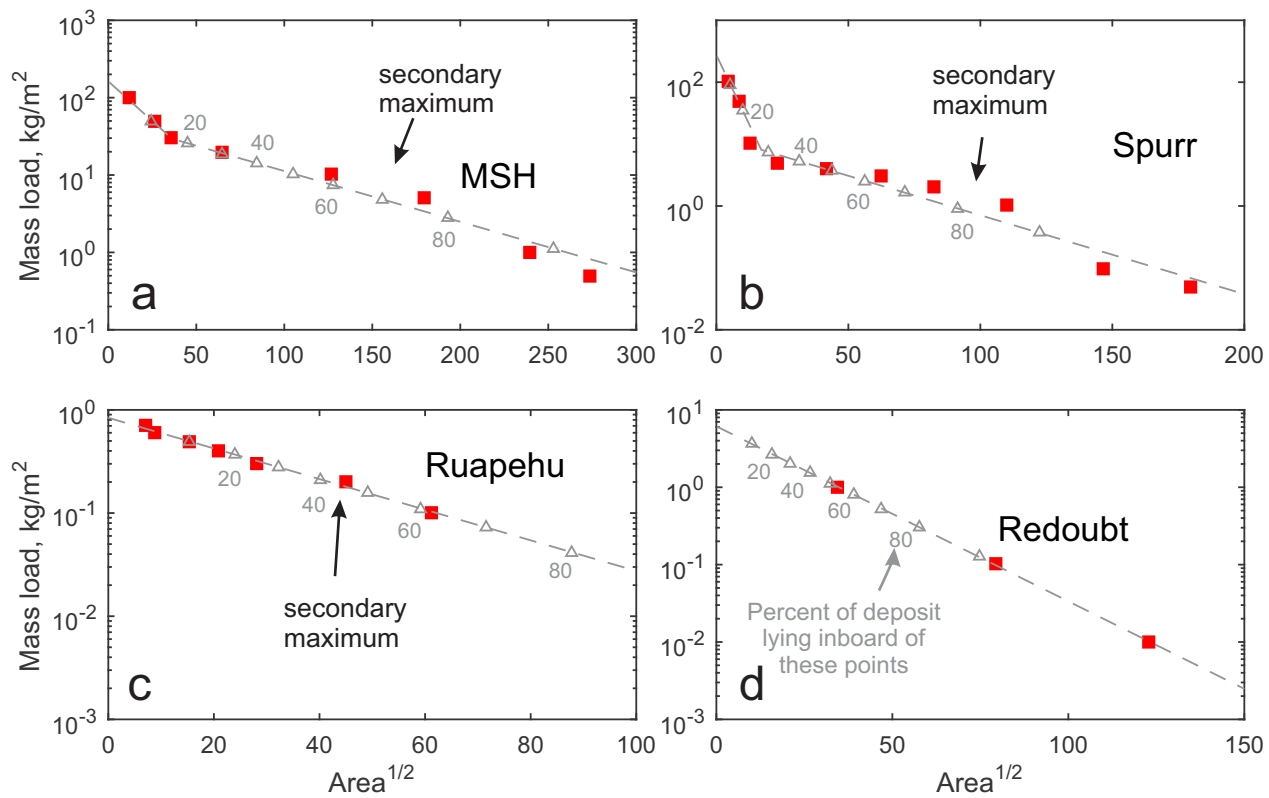


Figure 5

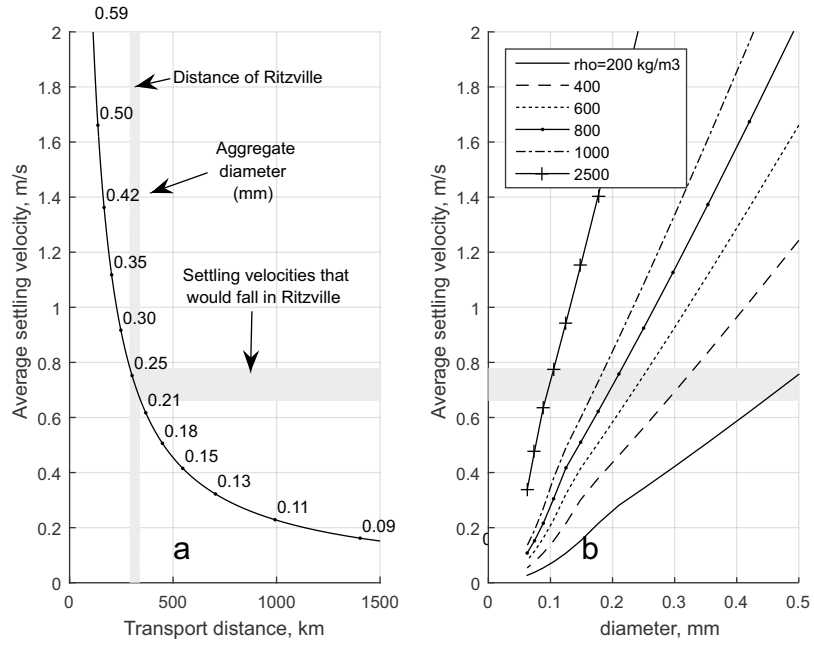


Figure 6

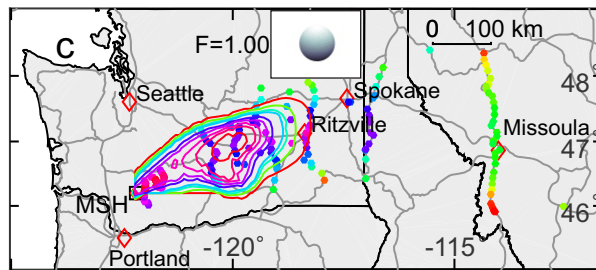
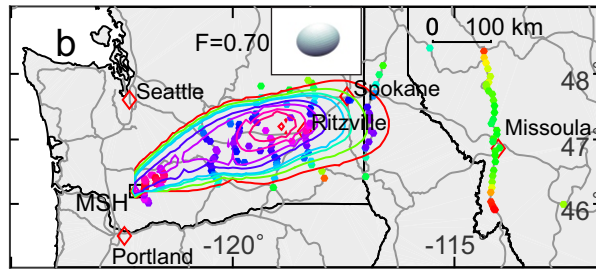
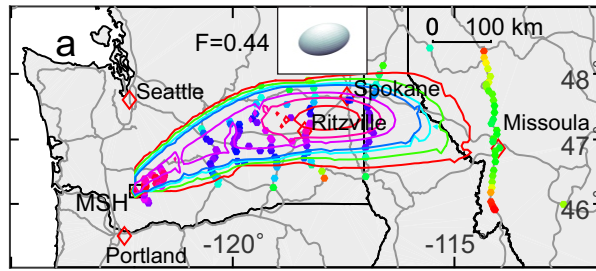


Figure 7

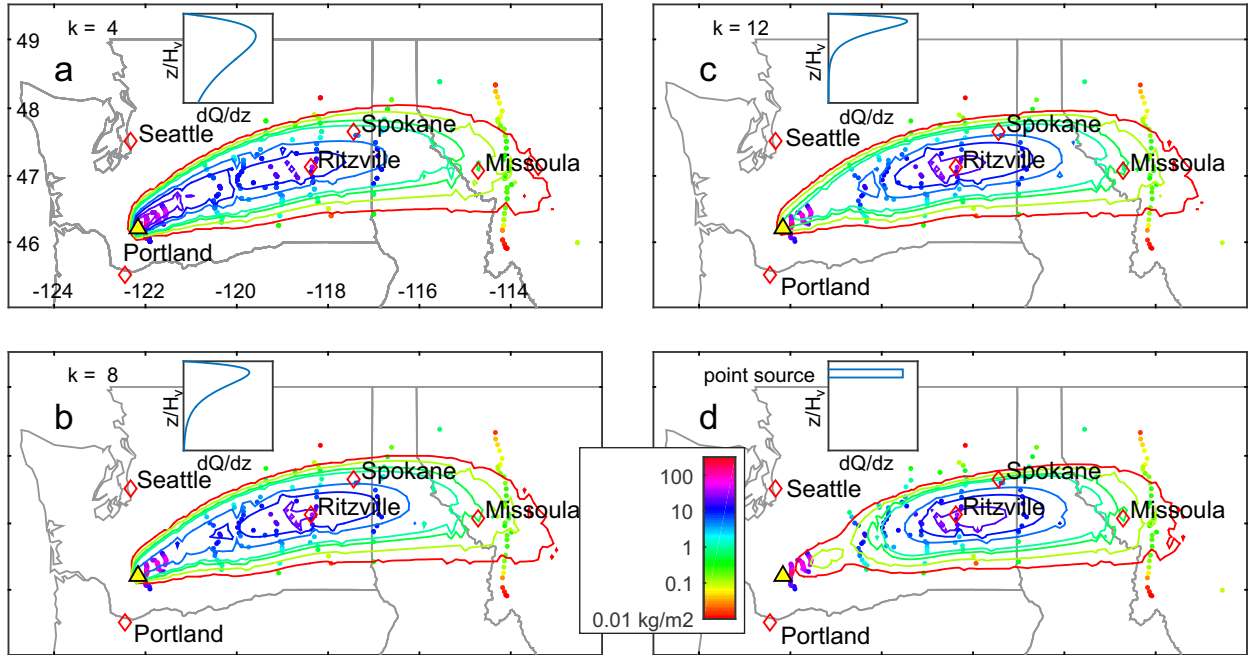


Figure 8

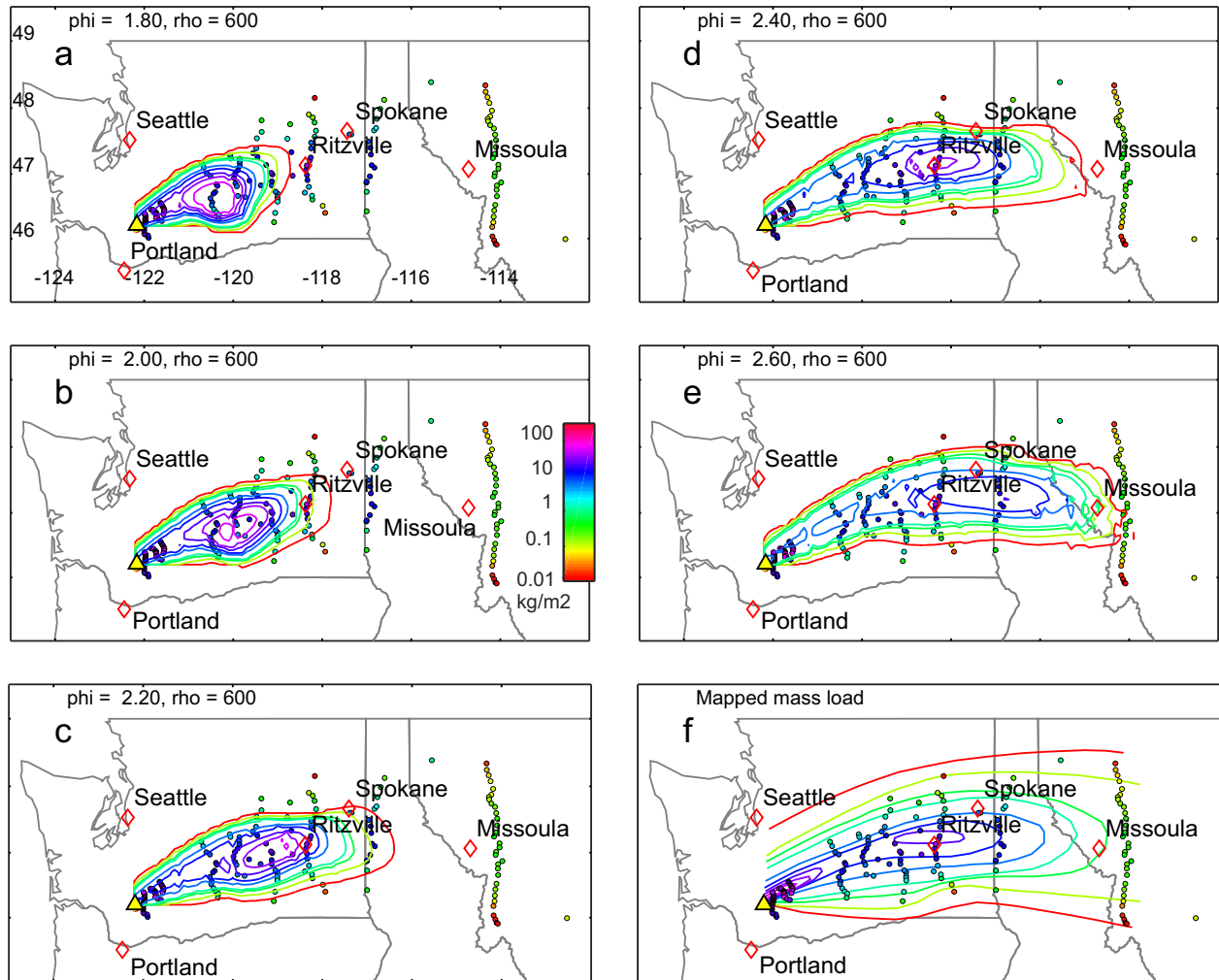


Figure 9

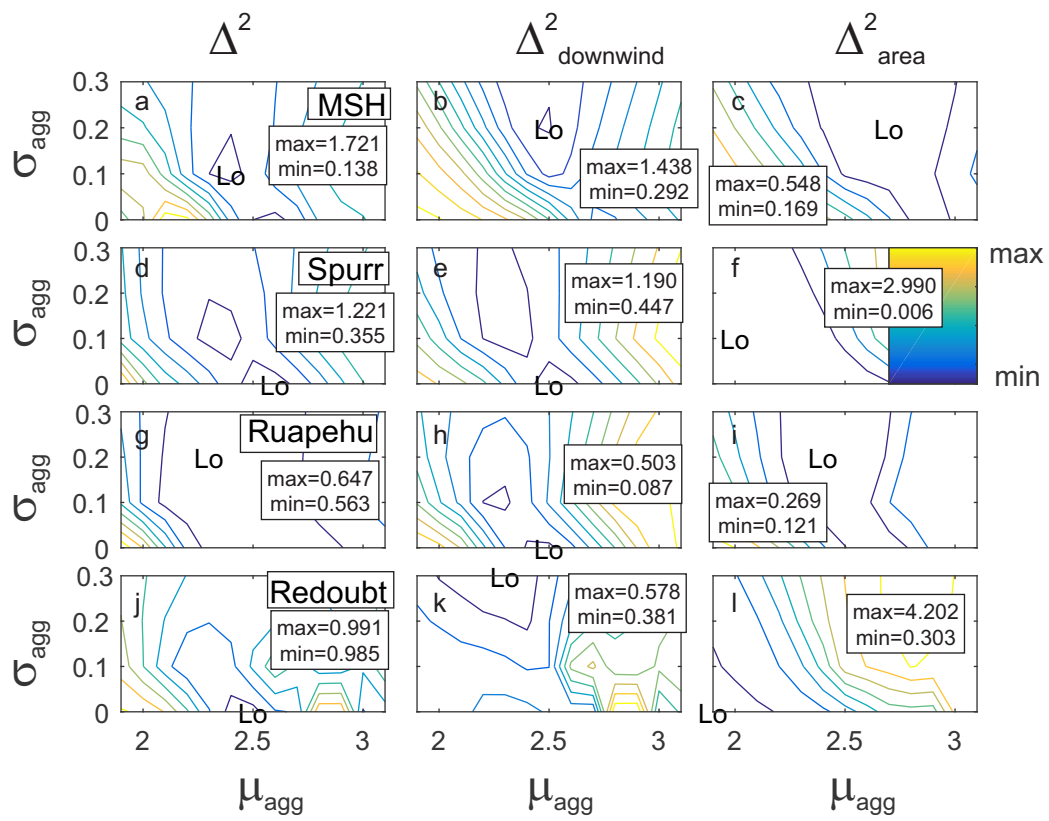


Figure 10

Mount St. Helens simulation, $\mu_{agg}=2.4\phi$, $\sigma_{agg}=0.1\phi$

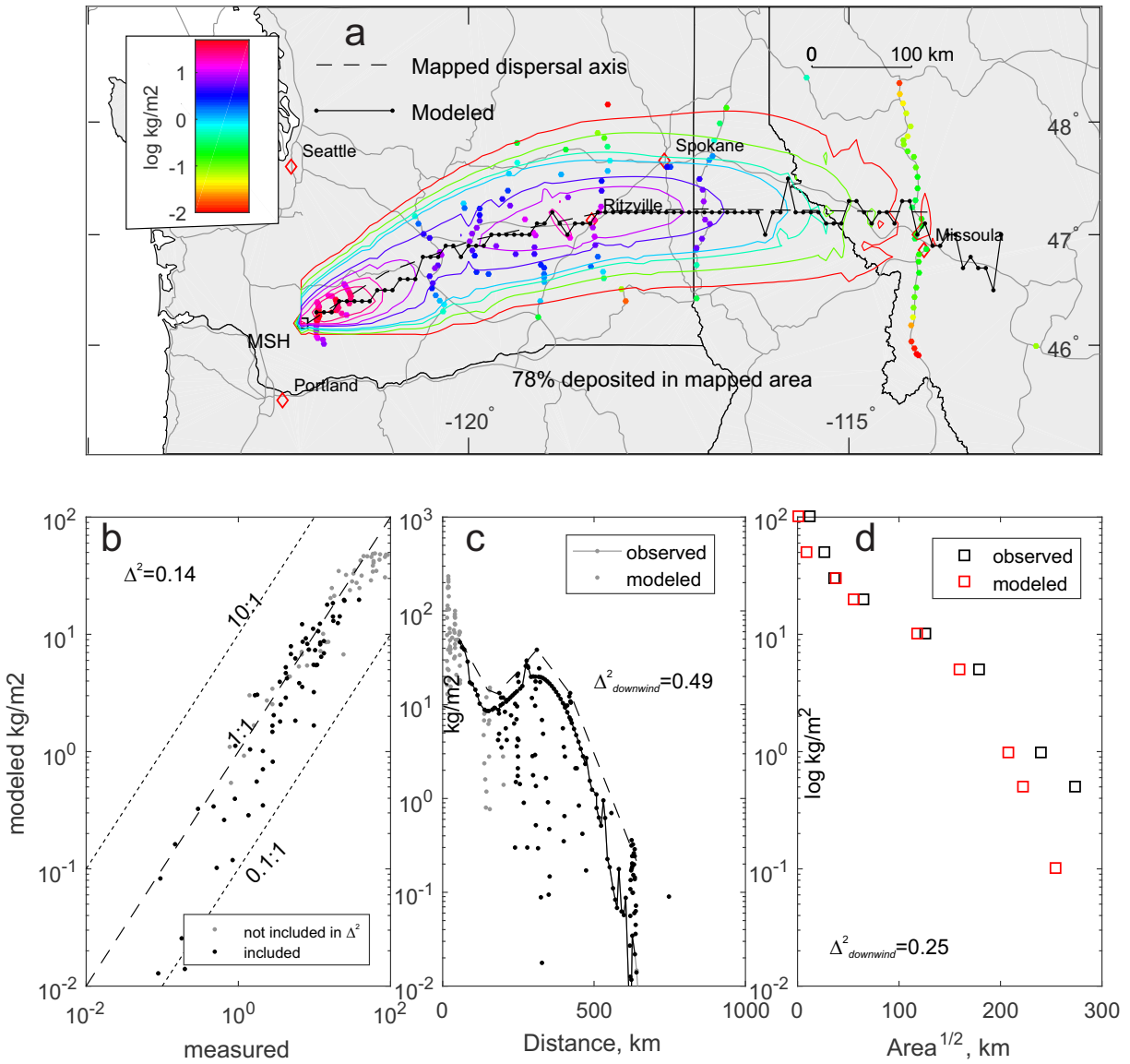


Figure 11

Crater Peak simulation, $\mu_{agg}=2.4\phi$, $\sigma_{agg}=0.1\phi$

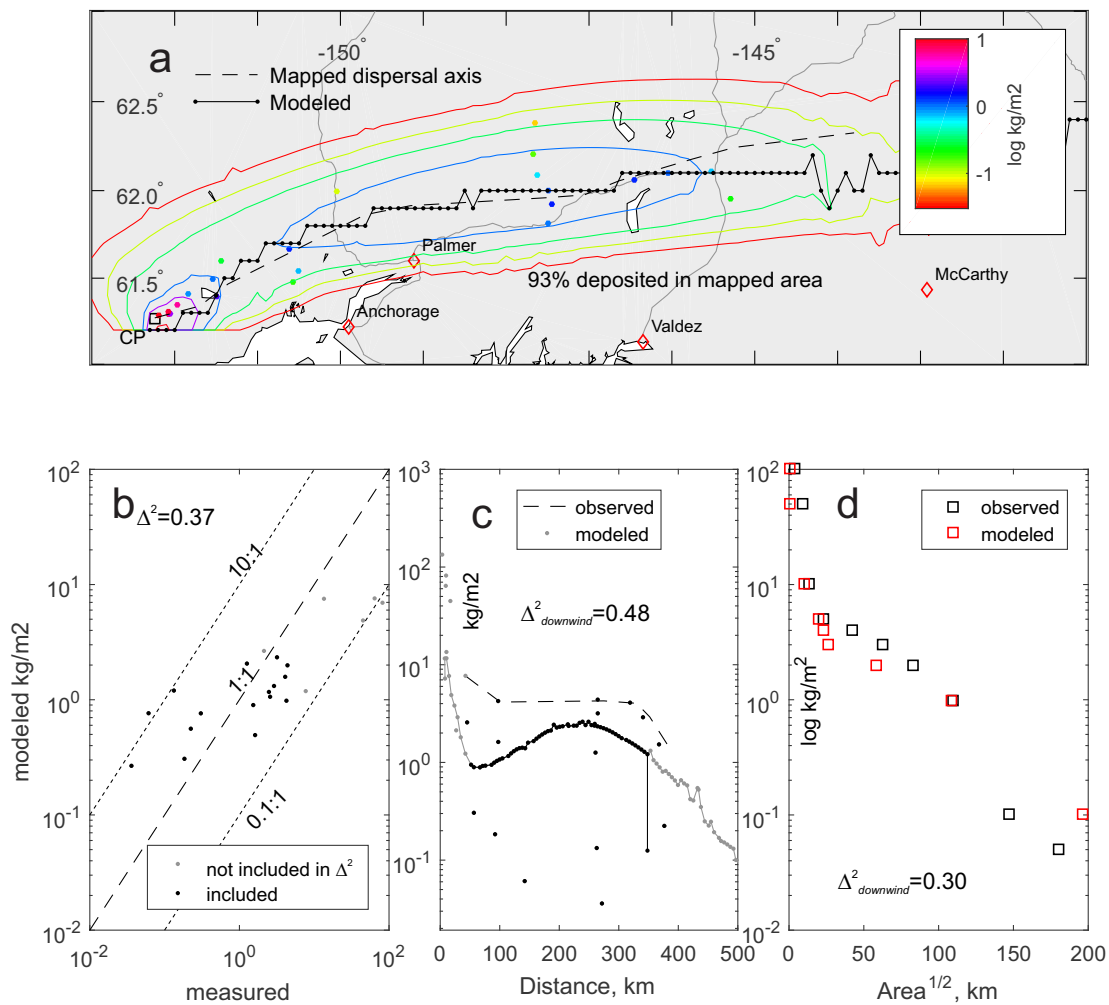


Figure 12

Ruapehu simulation, $\mu_{agg}=2.4\phi$, $\sigma_{agg}=0.1\phi$

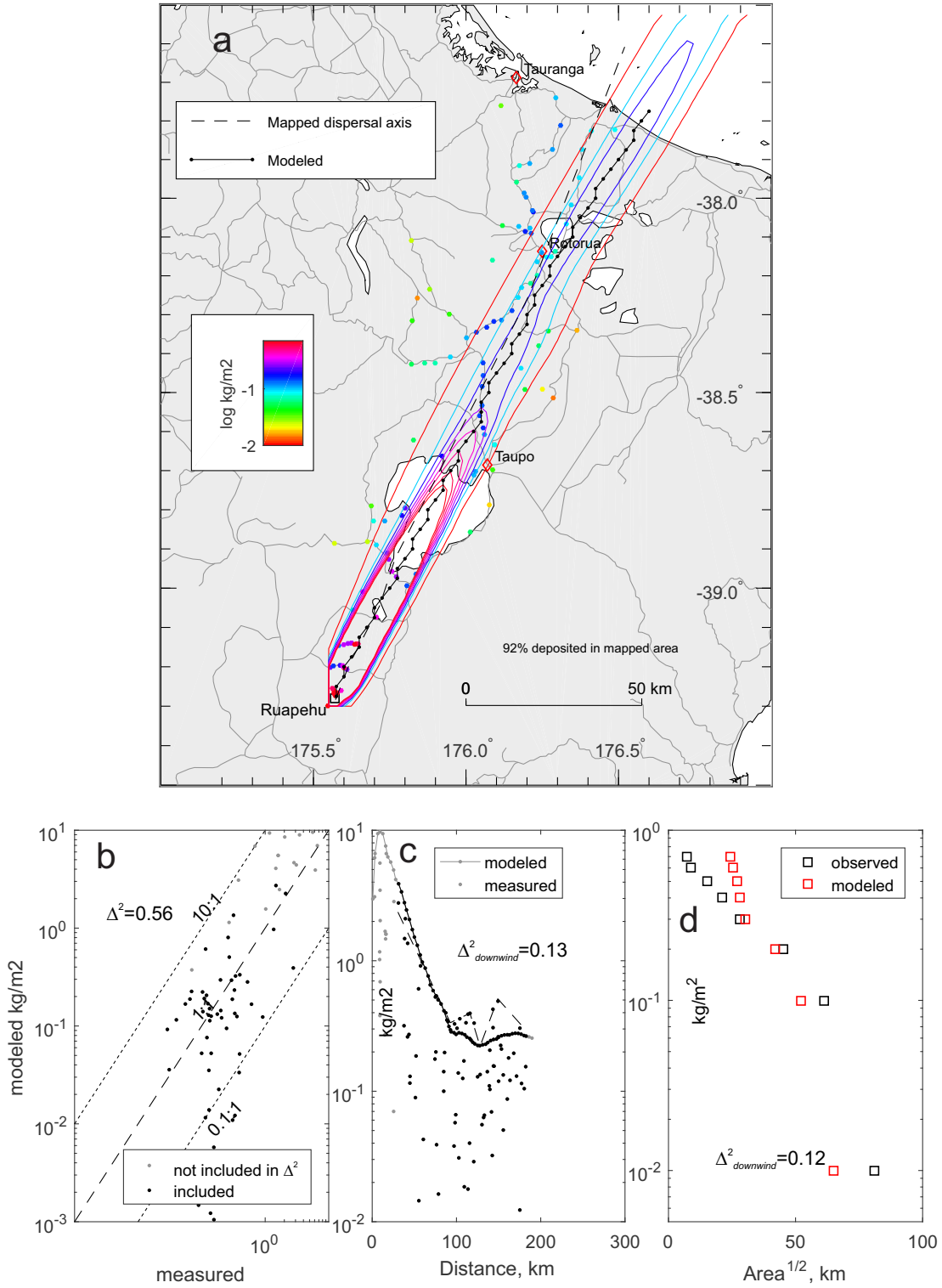


Figure 13

Redoubt simulation, $\mu_{agg}=2.4\phi$, $\sigma_{agg}=0.1\phi$

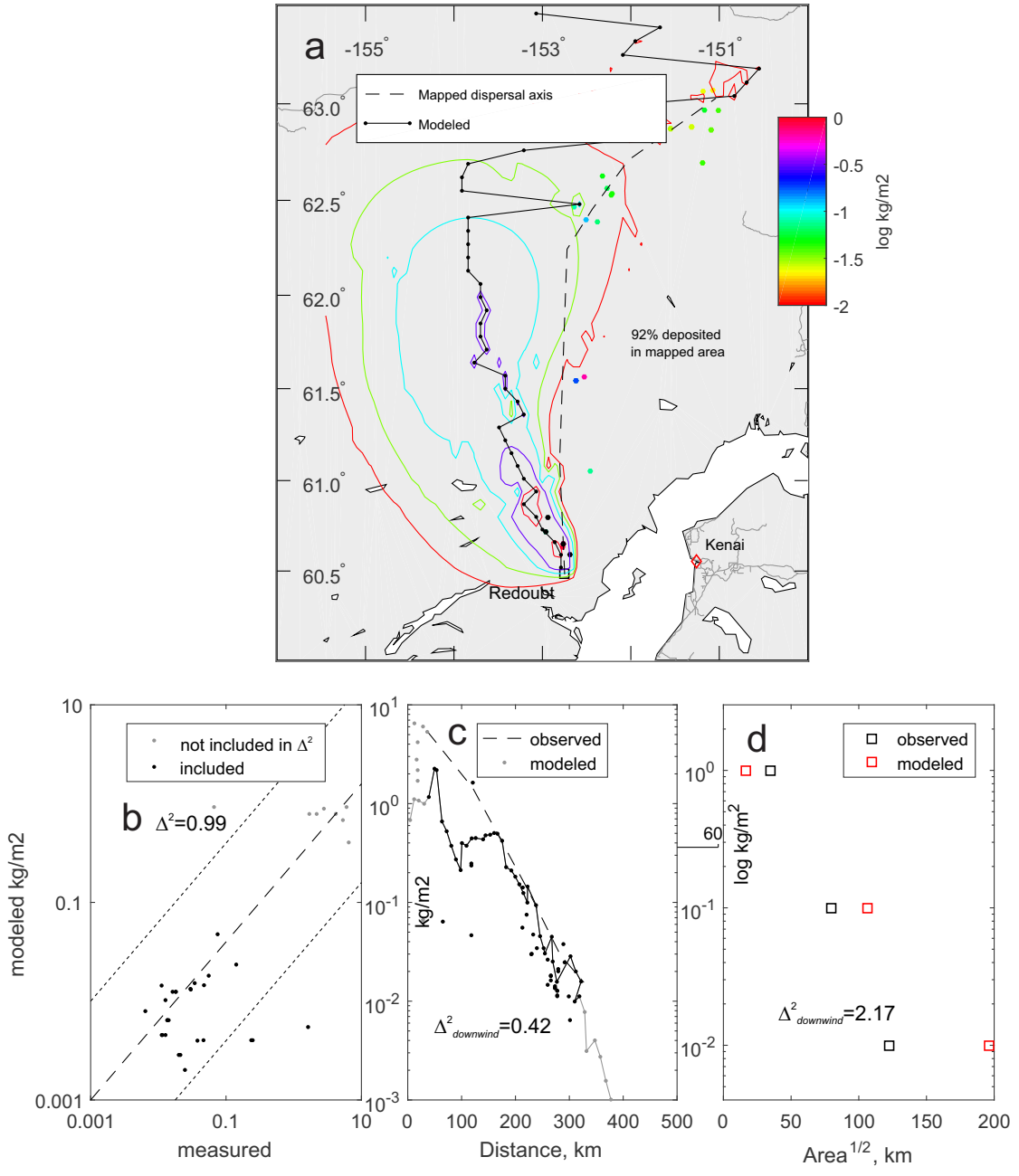


Figure 14

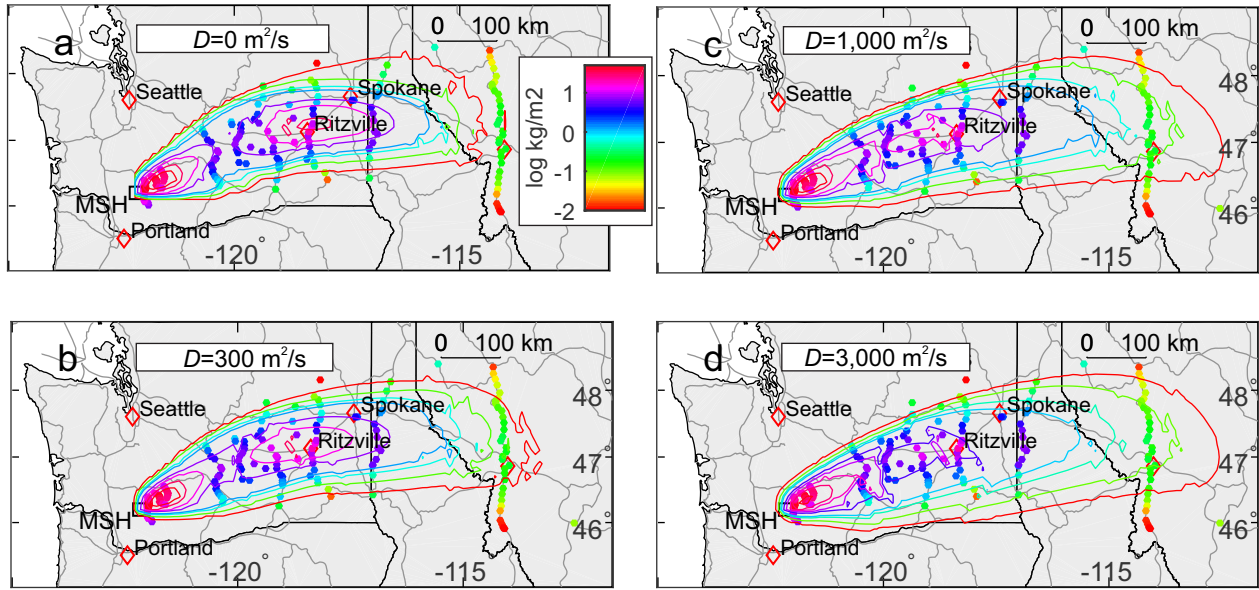


Figure 15

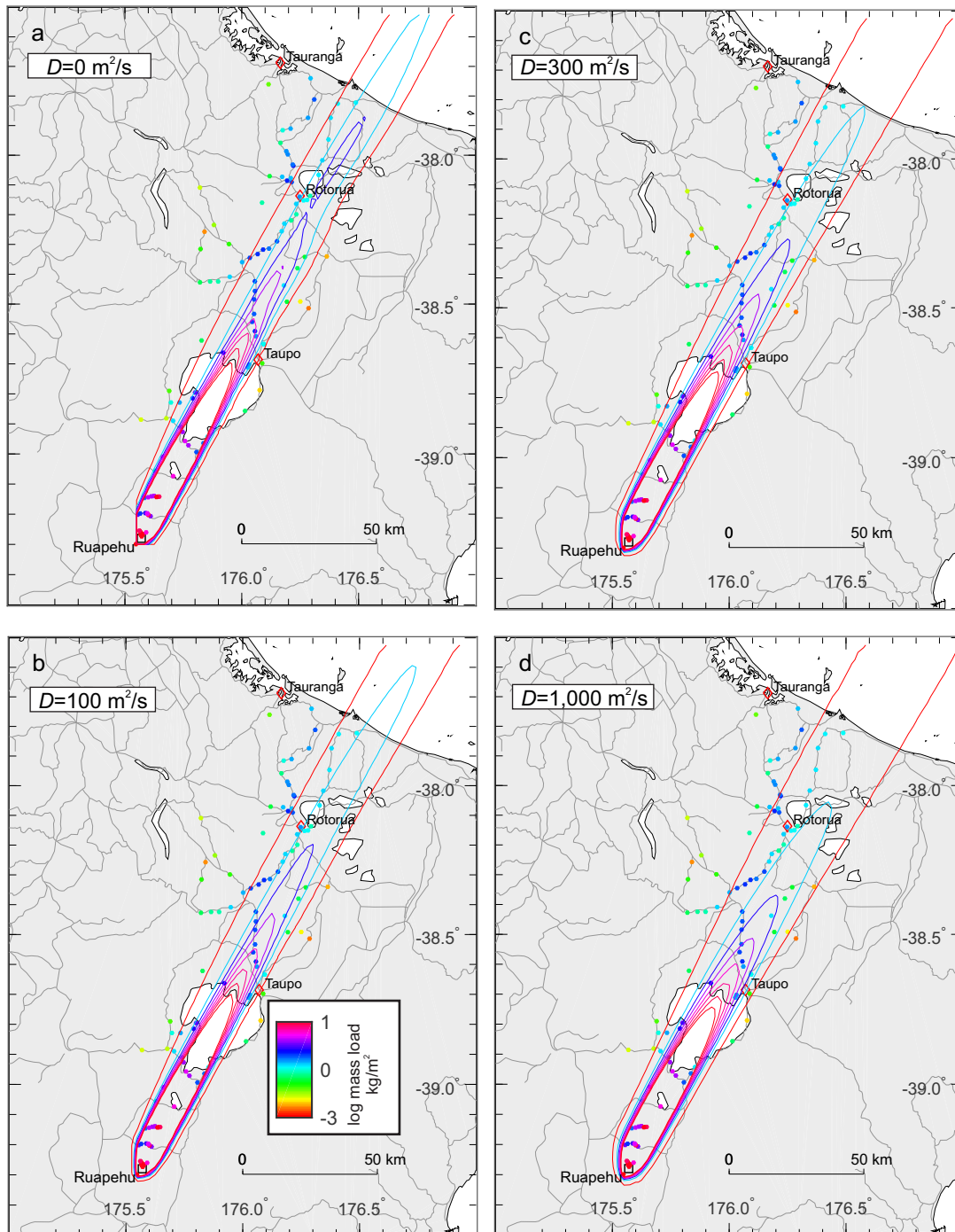


Figure 16